FINITE-DIFFERENCE TIME-DOMAIN (FDTD) SIMULATIONS AND FABRICATION OF A FABRY-PEROT CAVITY USING PHOTONIC CRYSTAL ARRAYS

by

JAE HWAN (ERIC) KIM

B. A. Sc., Kyung-Pook National University, 2001

A THESIS SUBMITTED IN PARTIAL FULFILMENT OF

THE REQUIREMENTS FOR THE DEGREE OF

MASTER OF APPLIED SCIENCE

in

THE FACULTY OF GRADUATE STUDIES

(Electrical and Computer Engineering)

THE UNIVERSITY OF BRITISH COLUMBIA

September 2007

Abstract

In this thesis, Fabry-Perot (FP) cavity structures aimed at a 850nm wavelength are modeled and analyzed by Finite-Difference Time-Domain (FDTD) simulations, for the purpose of fabricating resonant cavity detectors and Vertical-Cavity Surface-Emitting Lasers (VCSELs). The structures are based on square-lattice photonic crystals.

In designing a VCSEL, different types of highly reflective mirrors such as GaAs / AlGaAs Distributed Bragg Reflectors (DBRs), and a GaAs-based Sub-Wavelength Grating (SWG) or a Photonic Crystal (Phc) Slab are used to form a FP cavity. FDTD phase analysis is implemented to estimate resonant conditions in a simple but very effective technique.

For the fabrication of a resonant cavity detector, square-lattice photonic crystal arrays are written by (1) Focused Ion Beam (FIB) and (2) e-beam lithography, followed by dry-etching. The quality of air holes, etching depths, and sidewalls are scrutinized by Scanning Electron Microscopy (SEM) imaging and Atomic Force Microscopy (AFM). Post-patterning, a sacrificial layer is etched away by Buffered Oxide Etch (BOE) and a suspended photonic crystal membrane is released by Critical Point Drier (CPD).

The SWG and Phc slab used as one of the mirrors in the FP cavity structures are beneficial for achieving a compact-sized resonator, as well as forming multi-wavelength arrays, in which the resonance can be widely tuned by lithographically defined parameters (i.e., for the SWG: period and duty factor and for the Phc slab: lattice constant and radius of the air hole).

Table of Contents

Abstract....ii

List of Tables....v

List of Figures....vi

Acknowledgement....xii

Co-Authorship....xiii

Chapter 1. Introduction....1
  1.1 Author's contributions to the field....1
  1.2 Literature review....1
    1.2.1 VCSELs overview....1
    1.2.2 Tuable VCSELs....4
    1.2.3 Photonic crystal slab....6
    1.2.4 Resonant cavity detector....11
  1.3 Motivation....12
  1.4 Thesis overview....14
References....16

Chapter 2. DBR, Sub-wavelength grating, and Photonic crystal slab Fabry-Perot cavity design using phase analysis by FDTD....22
  2.1 Introduction....22
  2.2 VCSEL structure....24
  2.3 Periodic reflectors....27
    2.3.1 Sub-wavelength grating....29
    2.3.2 Photonic crystal slab....33
  2.4 Resonance tunability....37
  2.5 Cavity design for a Phc VCSEL....41
  2.6 Conclusion....45
References....46

Chapter 3. Device fabrication....48
  3.1 Wafer specification....48
  3.2 Pattern writing on GaAs slab....48
    3.2.1 Focused Ion Beam (FIB)....49
    3.2.2 E-beam lithography & dry-etching....55
  3.3 Removal of a sacrificial layer....58
  3.4 Conclusion....60

References......61

Chapter 4. Conclusion and Future Work......63
4.1 Conclusion......63
4.2 Future Work......64
References......69

Appendices......70
Appendix A. Quantum efficiency of a resonant cavity detector......70
Appendix B. Cavity Q measurement techniques......73
References......77

List of Tables

Table 2.1. Resonant Wavelengths Estimated by Three Different Methods, and Corresponding Cavity Qs..27

Table 2.2. Resonant Wavelengths Estimated by Two Different Methods, and Corresponding Cavity Qs..33

Table 2.3. Resonant Wavelengths Estimated by Two Different Methods, and Corresponding Cavity Qs..37

Table 2.4. Three different VCSEL structures aimed at the 850nm resonant wavelength..37

Table 3.1. Photonic crystal patterns with varying line doses and a probe current of SEM..55

Table 3.2. Etch rates with varied flow rate of BCl_3..57

Table 4.1. Emission wavelengths from fluorophores..67

List of Figures

Fig. 1.1. DBR stopband, measured by FDTD simulations and Transfer Matrix Method.........3

Fig. 1.2. A top-emitting cantilever VCSEL. Resonance tuning is done by the application of a voltage to control the cantilever.........5

Fig. 1.3. (a) Light propagates along with the air path made in photonic crystals and (b) various types of defects are created to strongly localize light.........7

Fig. 1.4. (a) Transmission and (b) reflection spectra of a single Phc slab after a plane wave is vertically incident to the slab.........8

Fig. 1.5. (a) Electric field amplitude recorded in a time monitor for transmission measurement and (b) Fourier transformation of the amplitude.........9

Fig. 1.6. The effect of the radius of the air hole on transmission spectra.........10

Fig. 1.7. (a) A schematic of square-lattice photonic crystal arrays on a single wafer for multi-wavelength selective emission or detection, and (b) a design example of arrays to detect wavelengths from 830nm to 860nm, while maintaining cavity Qs higher than 1,000.........14

Fig. 2.1. (a) A simple diagram of a FP cavity assuming for normal incidence. Resonances occur when the roundtrip inside a cavity is a multiple of $2\pi m$ ($m = 0, \pm 1, \pm 2 ...$) and (b) a

schematic diagram of a simple VCSEL structure forming a FP cavity……23

Fig. 2.2. Resonant wavelengths of the VCSEL structure for various cavity lengths (*L*) estimated by (a) the phase analysis and (b) the notch reflectivity in the DBR stopband……27

Fig. 2.3. The schematic diagram of two VCSEL structures, consisting of the air gap, 27.5 DBR pairs, and (a) the SWG and (b) the Phc slab forming the FP cavity……29

Fig. 2.4. (a) Reflectivities and (b) phases of a single SWG as varying the duty factor (A→C) and the period (C→E)……31

Fig. 2.5. (a) Phase responses of the SWG VCSEL and (b) resonant wavelengths shown in the DBR stopband as the duty factor (A→C) and the period (C→E) are varied……32

Fig. 2.6. (a) Reflectivities and (b) phases of a single Phc slab as the radius of the air hole is adjusted (A→B→C), and the lattice constant is varied (D→C→E)……34

Fig. 2.7. (a) Phase responses of the Phc VCSEL and (b) resonant wavelengths shown in the stopband under varying r (A→B→C) and a (D→C→E)……36

Fig. 2.8. (a) Tuning slopes of the three different VCSEL structures according to air gap

variation in the cavity and (b) corresponding cavity Qs at resonances..........................38

Fig. 2.9. Resonance tuning by (a) SWG duty factor (α), (b) SWG period (Λ), (c) Phc radius of the air hole (*r*) and (d) Phc lattice constant (*a*)..39

Fig. 2.10. Cavity Qs at resonances for the SWG and Phc VCSEL, lithographically (α, Λ, *r*, *a*) tuned...40

Fig. 2.11. (a) The Phc VCSEL including a 130nm $Al_{0.12}Ga_{0.88}As$ spacer and a 480nm air gap as a cavity (DESIGN1), and (b) the 800nm air gap placed above 40.5 bottom DBR pairs for the cavity (DESIGN2)...42

Fig. 2.12. Resonance tuning of two cavity designs by (a) varying *r* (*a*=446nm) and (b) changing *a* (*r*=0.48*a*)..43

Fig. 2.13. Cavity Qs of two cavity designs at resonances by (a) varying *r* (*a*=446nm) and (b) changing *a* (*r*=0.48*a*)..44

Fig. 3.1. A schematic of the wafer for a Phc VCSEL structure, based on Design 1 in Section 3.5...48

Fig. 3.2. (a) Formation of a single hole by putting small dots inside and (b) 5 x 5 array design...50

Fig. 3.3. (a) First trial of writing square-lattice (*a*=446nm and *r*=170nm) photonic crystal patterns with a 1.5microseconds dwell time and (b) zoom-in of the

holes.....51

Fig. 3.4. (a) Surface scanning of the patterns and (b) etching depth of a hole using AFM.....51

Fig. 3.5. Drilling is repeated as an addition of sequences (1)→(4).....52

Fig. 3.6. SEM images of 25 photonic crystal arrays after milling with a dwell time of (a) 0.5 microseconds, (b) 0.7 microseconds, (c) 1 microseconds, and (d) 1.5 microseconds.....53

Fig. 3.7. (a) Top view of overlapping, (b) cross section of holes with 1 microseconds dwell time and 5 loops, (c) Top view of overlapping and (d) cross section of holes with 0.5 microseconds dwell time and 5 loops.....54

Fig. 3.8. A square lattice of photonic crystal patterns after e-beam lithography. The size of each square is 80um x 80um.....56

Fig. 3.9. SEM images of holes designed for a=446nm and r=180nm taken after dry-etching.....57

Fig. 3.10. Measurement of the depth of a hole by AFM scanning.....58

Fig. 3.11. SEM images show a suspended membrane after BOE & CPD.....59

Fig. 3.12. Membranes are broken after BOE & CPD (sample made by e-beam &

dry-etching)..59

Fig. 3.13. Membranes are broken and lifted off after BOE & CPD (sample made by FIB mlling)..60

Fig. 4.1. Patterns are written onto the "C" shaped square..64

Fig. 4.2. E-beam lithography & dry-etching after removal of the sacrificial layer..65

Fig. 4.3. A proposed new wafer design. $Al_{0.3}Ga_{0.7}As$ and GaAs are used for the Phc slab and the sacrificial layer, respectively..66

Fig. 4.4. (a) A sharp resonance peak at 553nm is observed over the DBR stopband, 540nm to 560nm. The resonant detector design is based on AlN/AlGaN DBRs with a AlGaN Phc slab and (b) an example of DBM for the emission wavelength at 450nm and 590nm..67

Fig. A.1. The structure of the resonant cavity detector for analysis..70

Fig. B.1. (a) The log-scaled envelop of field decays recorded in a time monitor and (b) zooming in the envelop..73

Fig. B.2. (a) A schematic of the VCSEL structure with increasing cavity length to $20\lambda_{design}$

and (b) resonant frequencies shown in the stopband...75

Acknowledgements

First of all, my deepest appreciation goes to my supervisor, Dr. Lukas Chrostowski who has been always with me to solve obstacles and to improve results. His friendly guidance and fruitful advice have been most priceless to me for conducting and finalizing this project. His leadership to guide lab members leads to a successful teamwork and collaboration. As well, I am very happy to publish two papers with him and to be a presenter of the LEOS conference, which are among the most memorable moments in my life.

This research has been done in collaboration with Professor D.V. Plant and Dr. Eric. B at McGill University, and their comments and discussions are really helpful to progress my thesis. As well, I would like to appreciate Mario Beaudoin, Behnam Faraji, Yiyi Zeng, and Samantha Grist for their help and cooperation to do the fabrication work.

Finally, I would like to thank my father (Sang Soo Kim), my mother (Bu Ja Gong), my brother-in-law (Jae Guang Jung), my sisters (Hyun Jung Kim and Joo Yeon Kim), and my lovely nieces (Yeo Won Jung and Sae Bom Jung), and my soul mate, M. M for their mental support and encouragement.

Co-authorship

Jae Hwan (Eric) Kim conducted research, designed FP cavity structures based on a phase methodology, fabricated devices, and provided the first draft of the manuscript.

Professor D.V. Plant and Dr. Eric. B at McGill University provided a GaAs/AlGaAs wafer, set up the measurement system, performed experiments, and analyzed the optical response from SWGs and Photonic crystal slabs.

Yiyi Zeng and Samantha Grist performed the pattern writing on a GaAs wafer using dry-etching and FIB milling methods.

Dr. Lukas Chrostowski provided Lumerical solutions to perform FDTD simulations and guided to write the manuscript.

Chapter 1. Introduction

1.1. Author's contributions to the field:

1. First proposal of a FP cavity design with a photonic crystal slab
2. Proposal of resonance tuning by lithographic control in a Phc FP cavity.
3. J. Kim and L. Chrostowski, "Fabry-Perot Cavity Design in AlGaAs/GaAs using a Photonic Crystal Slab for a Resonant Cavity Detector," *Lasers and Electro-Optics Society Conference*, Oct. 2006.
4. J. Kim, L. Chrostowski, E. Bisaillon, and D.V. Plant, "DBR, Sub-wavelength grating, and Photonic crystal slab Fabry-Perot cavity design using phase analysis by FDTD," Optics Express. **15**, 10330-10339, 2007.

1.2. Literature Review

1.2.1. VCSELs overview

The Vertical-Cavity Surface-Emitting Laser (VCSEL) is now a key optical source in fiber optic communications, due to its outstanding capabilities. Various advantages of using the VCSEL include easier fiber coupling, ultra-parallel information transmission, dynamic single-mode operation, fabrication in arrays, as well as easy packing, bonding, and mounting, etc. [1-3]. In particular, compared to conventional stripe lasers, the VCSEL has a distinctive feature in terms of a relatively low threshold current as a result of reducing the volume of the active region [3].

The VCSEL consists of two Distributed Bragg Reflectors (DBRs), epitaxially grown, and an optical cavity, typically a single wavelength thick. An active region is located inside the cavity where multiple quantum wells are placed. The location of the quantum wells is overlapped with the antinode of the standing wave in order to maximize the modal gain [1].

DBRs are composed of multiple pairs of quarter-wavelength-thick high- and low-refractive index materials, with the choice of materials dependent on the lasing wavelength. Some distinctive benefits of using DBRs are high and flat reflective span, also called *stopband*, by multi-pairs, and a relatively flat phase on reflection at the stopband. The width of the stopband is proportional to the refractive index difference between the two DBR materials, while reflectivities depend on how many pairs are used to form the DBRs.

In this DBR design, we set the design wavelength for DBRs to 850nm and use the following quarter-wavelength-thick DBR layers: 60.3nm thick $Al_{0.12}Ga_{0.88}As$ (n=3.53) and 70.1nm thick $Al_{0.9}Ga_{0.1}As$ (n=3.03). In Finite-Difference Time-Domain (FDTD), reflected fields from the DBR are recorded in a frequency monitor after a plane wave is incident on DBR. According to our FDTD results, in order to obtain more than 99% reflectivity from the DBR, more than 20 pairs are required, at least.

In Fig. 1.1, the shape of the DBR stopband is plotted from 40 DBR pairs, using FDTD simulations and the Transfer Matrix Method (TMM). In the FDTD simulation, a 2D or 3D physical structure is designed, boundary conditions along with the structure are set, electromagnetic source is defined, and frequency and time monitors are placed in specific locations where the transmission or reflection of the structure is measured. After the light is emitted toward the structure within the boundary, one can characterize the optical response. The Transmission matrix relates inputs and outputs of a single layer. Since multiple pairs are used to construct DBR pairs, a multi-port can be cascaded by transmission matrices. TMM is to calculate reflection and transmission coefficients of DBR pairs by relating each coefficient with scattering matrix [43].

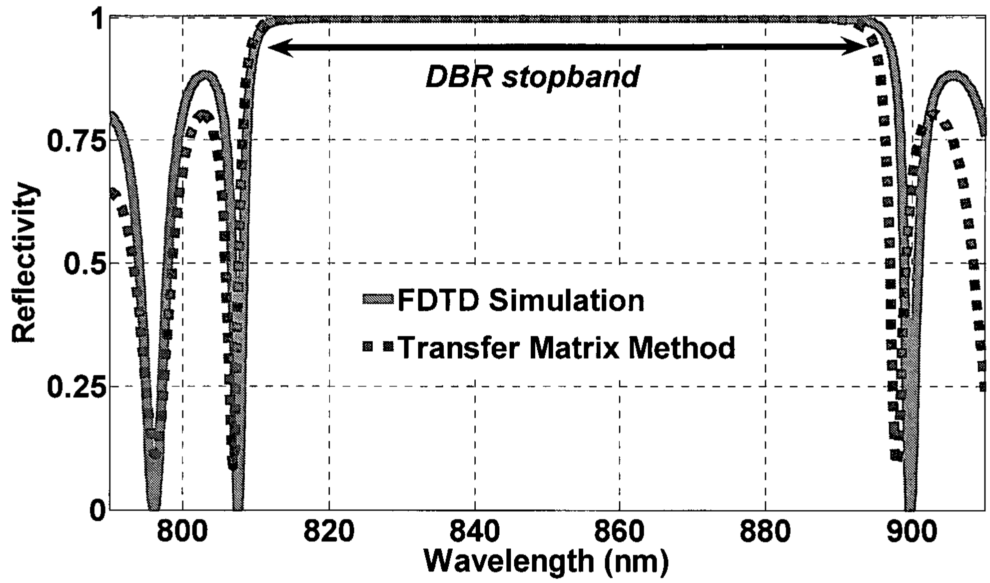

Fig. 1.1. DBR stopband, measured by FDTD simulations and Transfer Matrix Method.

Effective electrical and optical confinement is very important to the design of the VCSEL, and two VCSEL structures, a proton-implanted and an oxide-apertured VCSEL are widely used. For the proton-implanted VCSEL (also called gain-guided), ions implanted in the p-DBR region make the injected current directed toward the center of the active region (electrical confinement), while the thermal lensing effect confines the transverse optical mode (optical confinement). For the oxide-apertured VCSEL (also called index-guided), similar to the proton-implanted VCSEL, oxide layers help the injected current flow to the center of the active region (electrical confinement), while the relatively low refractive index of the oxide layers located above and below the active region confines the transverse mode (optical confinement).

1.2.2. Tunable VCSELs

As communication bandwidth is being tremendously increased in Dense Wavelength Division Multiplexing (DWDM), cost-effective but highly reliable ways to send and receive multiple channels are becoming more important. Several methods of achieving tunable VCSELs have been investigated extensively since 1989, once VCSEL layers could be more precisely deposited by such fabrication techniques as Molecular Beam Epitaxy (MBE) and Metalorganic Chemical Vapor Deposition (MOCVD) [4-8].

As VCSELs are fabricated in arrays, a first trial to emit multiple wavelengths by grading the thicknesses of layers was demonstrated in [9,10] and a series of pertinent works was reported in [11-16]. Different wavelengths can be emitted from the VCSEL arrays by grading two layers near the cavity layer [17]. Very precise epitaxial deposition is required to place the graded layers in this structure; otherwise, a minuscule miscalibration in the layer deposition gives rise to huge shifting of a design wavelength. In addition, the achievable tunable range is quite narrow, since the maximum gradient of the graded layers achievable by the non-uniform growth is limited.

MEMS-based cavity variation, operated by the application of an electrostatic force, would, in general, be superior to the thickness gradient in terms of resonance tunability.

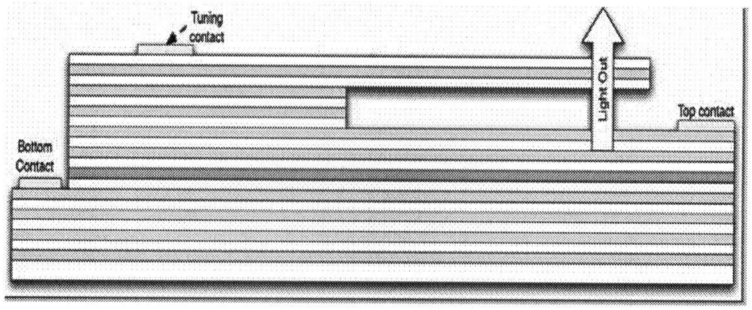

Fig. 1.2. A top-emitting cantilever VCSEL. Resonance tuning is done by the application of a voltage to control the cantilever.

One example of MEMS-based VCSELs is a top-emitting cantilever VCSEL as shown in Fig. 1.2. This structure consists of a bottom n-DBR, a cavity including a QW active region, and a top mirror (p-DBR, air gap, and n-DBR), with a tuning voltage applied to generate the electrostatic force [17]. As the reverse-biased voltage is increased, the cantilever moves down, which gives rise to a shortening of the air gap, resulting in blue shifting. The tunable range of this VCSEL structure is about 32nm, and the maximum movable range of the air gap is limited to 1/3 of the gap size, which is the structural limitation of capacitive MEMS structures. Various groups have designed different structures, such as a membrane-type [18] or a half-symmetry cavity MEMS-VCSEL [19], but the fundamental scheme of resonance tuning is the same; i.e., the electrostatic force attracts the top DBR down to achieve the blue shifting. A piezoelectrically actuated MEMS VCSEL could overcome the 1/3 air gap limitation and thus improve the tunable range of wavelengths [20], but it still needs a tuning voltage for piezoelectric actuation.

1.2.3. Photonic crystal slab

Photonic crystals are considered to be one of the most intriguing fields in photonics, due to their ability to maneuver the flow of light [21,22]. The basic idea is that periodic perturbation of dielectric materials gives a photonic band gap that waves can not propagate at certain wavelengths. The photonic bandgap is analogous to the energy bandgap where electrons are forbidden in a periodic array of atoms. Depending on the photonic band gap that is of interest and the polarization of the wave, air holes or rods can be created.

The first thinkable idea from the photonic crystals is a line defect; i.e., waveguide. When the light is emitted to photonic crystals, it is guided along the line defect as shown in Fig. 1.3(a). Out of the path are photonic crystals where light can not propagate. Comparing to the fiber-optic cables where light is guided by total internal reflection, waves can be completely guided in case of photonic crystals, regardless of the angle of the path light goes through. As well, defects made at certain points in the photonic crystals can strongly localize the light; i.e., cavity, as shown in Fig. 1.3(b). Defects can be created by removing, resizing, or relocating the holes. Due to strong localization of the light, the photonic crystal cavity provides a very high quality factor that could be used for laser applications.

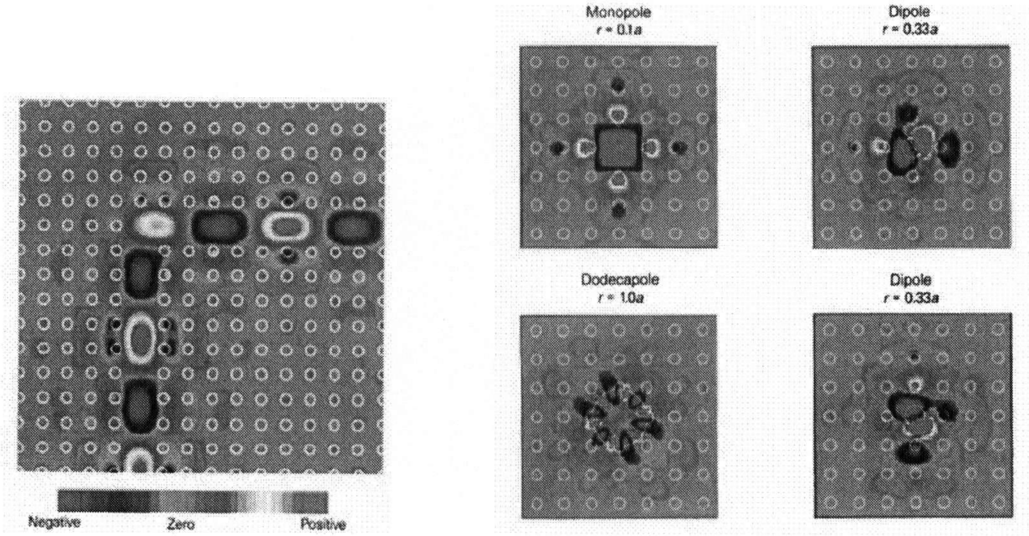

(a) (b)

Fig. 1.3. (a) Light propagates along with the air path made in photonic crystals and (b) various types of defects are created to strongly localize light (From reference [21]).

On the other hand, the characteristics of Photonic crystal (Phc) slabs, assuming the incident field emits normally to the slabs, have not been intensively exploited, in spite of their unique advantages in the design of filters [23,24]. As well, as described in [25,26], highly reflective mirrors can be obtained by proper settings of Phc parameters.

Depending on whether the Phc slab can couple to external radiation or not, the slab supports in-plane guided modes with an infinite lifetime, and guided resonances with a finite lifetime [27]. When the light is incident on the slab, in-plane guided modes are entirely bound to the slab without any coupling to external radiation, while guided resonances, also confined within the slab can couple to external radiation [27]. Upon modification of guided resonances, various features of transmission and reflection are obtainable.

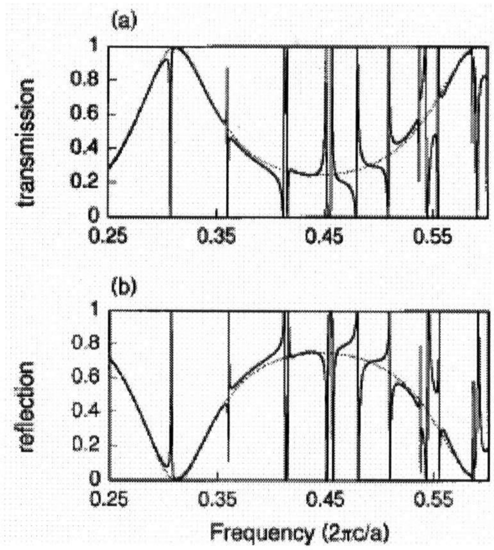

Fig. 1.4. (a) Transmission and (b) reflection spectra of a single Phc slab after a plane wave is vertically incident on the slab (From reference [27]).

Determining the transmission and reflection characteristics of a Phc slab is of significance for modeling of specific applications. In Finite-Difference Time-Domain (FDTD) simulations, we assume that a plane wave, having its electric field perpendicular to the plane of incidence, is emitted toward the Phc slab and that both frequency and time monitors are located above and behind the slab. In Fig. 1.4, the field amplitudes obtained by the frequency monitors are shown [27]. Dotted lines added on both plots represent a background reflectivity, which is measured from the slab containing no photonic crystal pattern. The guided resonances appear as sharp lines in transmission and reflection spectra, which are relatively complicated and asymmetric.

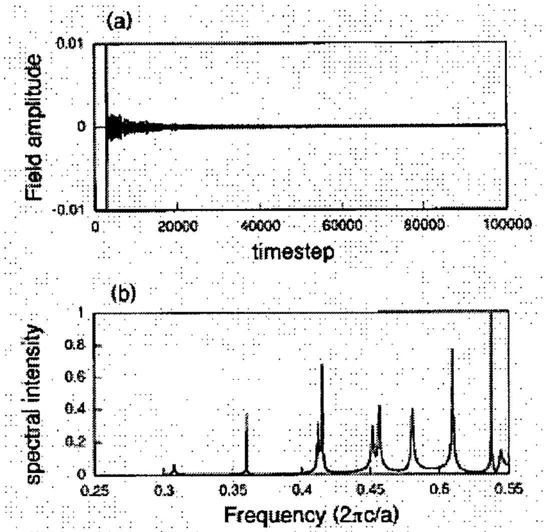

Fig. 1.5. (a) Electric field amplitude recorded in a time monitor for transmission measurement and (b) Fourier transformation of the amplitude (From reference [27]).

The electric field amplitudes are recorded in the time monitor as shown in Fig. 1.5(a), as a function of the timestep. After an initial pulse occurs, the amplitudes tend to gradually decay as the timestep increases. The first initial pulse shown is due to the slab background transmission (or reflection), representing the incident energy going directly to the slab and generating the initial pulse; this is called a *direct* transmission process [27]. As well, the remaining portion of the incident energy produces guided resonances, which is called an *indirect* transmission process. Several sharp peaks in Fig. 1.5(b) represent the guided resonances, which are achieved by Fourier transformation of the long decay amplitude [27].

The radius size of the air hole plays an important role in determining the Q factors of the guided resonances. As shown in Fig. 1.6, when the radius of the air hole is increased from $0.05a$ to $0.20a$, the Q factor of the guided resonance tends to be lower (reduced lifetime) [27].

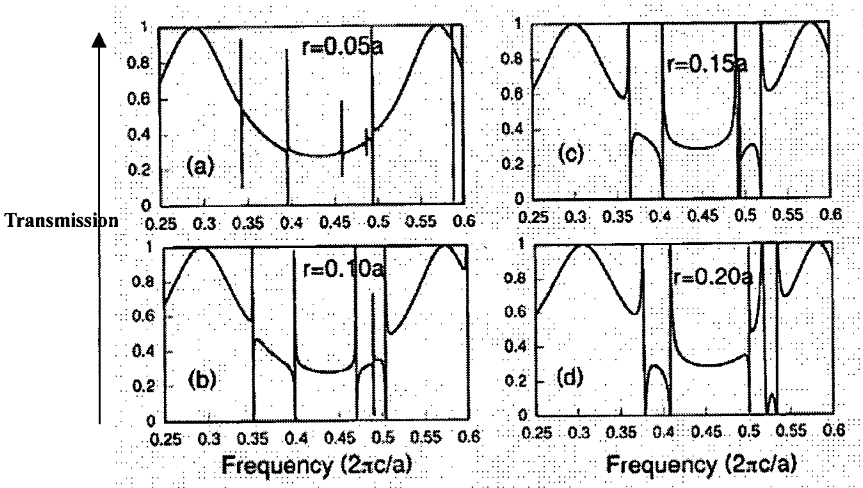

Fig. 1.6. The effect of the radius of the air hole on transmission spectra (From reference [27]).

Thus, when it comes to the filter design for specific wavelengths, smaller air holes (higher Q factors of the guided resonances) may be more suitable than larger holes. For the design of highly reflective mirrors, larger air holes (lower Q factors of the guided resonances) would be more appropriate to achieve high and wide reflectivity spans from the slab. This work in the thesis utilizes these high reflectivity peaks originating from the guided resonances, for values of *r* larger than shown in Fig. 1.6.

In Chapter 2, we demonstrate high reflectivities from the Phc slab after optimization of lithographic parameters. For the $Al_{0.12}Ga_{0.88}As$ used as the Phc slab material, the range of the radius of the air hole should be between 0.40*a* and 0.49*a*, in order to be used as a highly reflective mirror in a Vertical-Cavity Surface-Emitting Laser (VCSEL) structure.

1.2.4. Resonant cavity detector

A photodetector is a device to convert an optical signal into an electrical signal, in order to recover the data in fiber-optic communications. Semiconductor photodiode detectors are commonly based on a p-n junction, where a local electric field exists a depletion region. When the light is absorbed in the device, carriers are transported by the electric field over the depletion region, which contributes to a current flow in a reverse direction. For a p-i-n photodiode, an intrinsic layer is inserted between the p-n junction to increase the depletion area. Also, a faster carrier drift can be achieved by reducing the ratio between the diffusion and drift length [37-40].

The quantum efficiency (η), defined as a conversion ratio between photons and a pair of carriers for these conventional photodetectors, can be written as [37,41]

$$\eta = (1-R)\cdot\left[1-\exp(-\alpha d)\right] \tag{1}$$

where R = surface reflection, α = an absorption coefficiency, and d = the thickness of an active layer. Therefore, if a material with antireflection is specified, the only way to achieve higher quantum efficiency is to increase the thickness of the active layer. On the other hand, extending the active layer limits the device speed, as the transit time is also increased.

In this regard, a resonant cavity detector provides a conspicuous advantage in terms of achieving very high quantum efficiency (>0.99) with a very thin active layer [42]. As well, it enables selective detection of specific wavelengths, while a high quality factor at resonance can enhance the quantum efficiency. The work presumed in this thesis can be used to fabricate multi-wavelength detector arrays with improved quantum efficiency.

1.3. Motivation

Recently, several groups have suggested that Sub-Wavelength Gratings (SWGs) can provide very high reflectivities and can therefore replace one of the DBR pairs [28-31]. In particular, a VCSEL incorporating a high index-contrast SWG was demonstrated [30], indicating that a SWG-MEMS VCSEL is possible for a wide range of tunable wavelengths.

When the VCSEL or the resonant detector includes the SWG as a highly reflective mirror, our analysis indicates that the total phase response of the structure can be changed by variation of lithographically defined SWG parameters, a period (Λ) and a duty factor (α), rather than by the cavity length. This technique represents another method of tuning the resonant wavelength lithographically. The emission (or detection) of multiple wavelengths is thus possible by SWG arrays [28].

Similar to SWGs, a Phc slab can also provide very high and wide reflectivities [32,33] by proper settings of the slab thickness and lithographically defined parameters, such as the lattice constant (a) and the radius of the air hole (r). This thesis is motivated by the feasibility of high and wide reflectivities from the Phc slab, which can successfully replace one of the DBR pairs in tunable structures (VCSEL or resonant detector).

Various groups have demonstrated photonic-crystal VCSEL structures, aiming to the single mode operation and control of output polarization [34-36], however, in this case, the photonic crystal arrays are patterned onto the top DBR pairs. The design goal in this thesis is for the replacement of one of DBRs using a Phc slab for a compact-sized VCSEL as well as lithographic resonance tuning, which are distinguishable from the Photonic Crystal VCSELs published earlier.

Several fruitful benefits of using the Phc slab are as follows:

1. Phase change is possible by variation of lithographic parameters, implying lithographic tunability of the lasing or resonant wavelength.
2. Fabrication recipes and techniques of GaAs / AlGaAs used for the Phc slab, the sacrificial layer, and the DBR pairs are well known and widely used.
3. The membrane of the Phc slab can be more robust than that of the SWGs.
4. A more compact-sized resonator is possible as a result of replacing one of the DBRs (~4um) with the Phc slab (~250nm).
5. Multi-wavelength emission or selective detection is possible by photonic crystal arrays.

Fig. 1.7(a) illustrates a multi-wavelength emission or selection by writing square-lattice photonic crystal arrays on a wafer. As exemplified in Fig. 1.7(b), specific resonant wavelengths with relatively high-cavity Qs can be designed by the appropriate choice of a lattice constant (*a*) and the radius of the air hole (*r*) in the array.

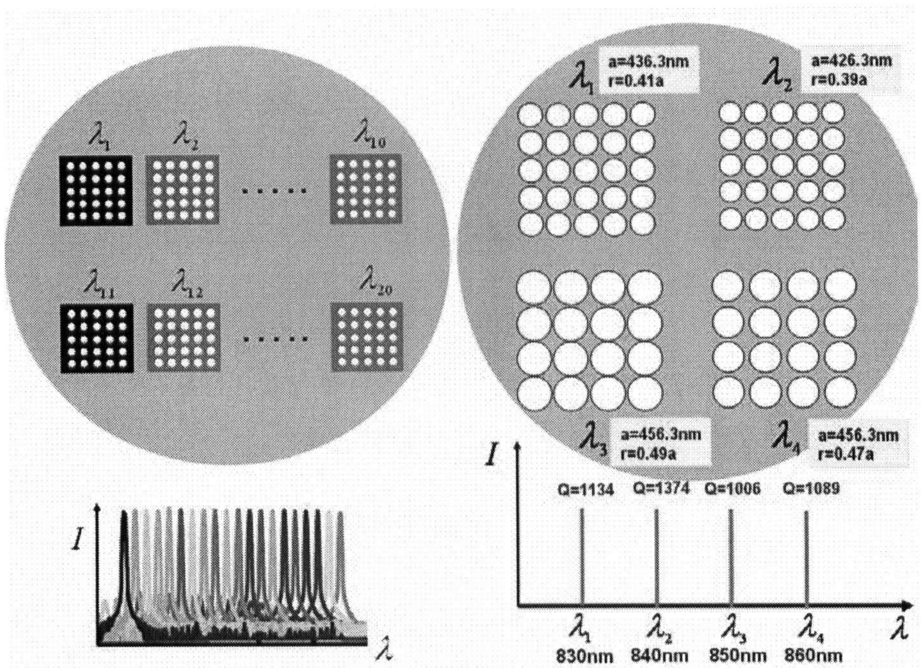

(a) (b)

Fig. 1.7. (a) A schematic of square-lattice photonic crystal arrays on a single wafer for multi-wavelength selective emission or detection, and (b) a design example of arrays to detect wavelengths from 830nm to 860nm, while maintaining cavity Qs higher than 1,000.

In addition to DWDM, this structure can be applied for detection of emission wavelengths from fluorescent molecules. Emission wavelengths of Fluorophore are ranging from 425nm to 670nm, so proper settings of GaN and AlGaN for DBRs and a Phc slab can be used for optical biosensing devices.

1.4. Thesis Overview

Chapter 2 is a manuscript that has been published in *Optics Express*. In this manuscript, a phase methodology to predict a resonant wavelength in a conventional VCSEL structure is demonstrated, and the results are validated by FDTD reflectance and the Transfer Matrix

Method (TMM). The FDTD phase method is extended to a SWG and a Phc slab for analysis of their reflectivity and phase responses, and resonance tunability of a SWG VCSEL and a Phc VCSEL. Finally, a lithographic resonance tunability is studied to achieve a wide tuning range.

Chapter 3 describes the fabrication procedures to make square-lattice photonic crystal arrays on a GaAs wafer. The quality of patterns written by FIB and e-beam & dry-etching, sidewalls of air holes, and suspended membranes made by BOE & CPD are carefully investigated by SEM imaging. Optimum parameters and the most suitable settings for device fabrication are suggested.

Chapter 4 summarizes the work and the results achieved, and suggests future work to improve and continue device fabrication / experimental measurements.

References

[1] H. Li et al., "Vertical-Cavity Surface-Emitting Laser Devices," Springer, 2002.

[2] S. F. Yu, "Analysis and Design of Vertical Cavity Surface Emitting lasers," Wiley, 2003.

[3] C. J. Chang-Hasnain, "Tunable VCSEL," IEEE Journal on selected topics in Quantum Electronics, vol. 6, no. 6, 2000.

[4] W. Yuen, G. S. Li, and C. J. Chang-Hasnain, "Multiple-wavelength vertical-cavity surface-emitting laser arrays," IEEE J. Select. Topics Quantum Electron., vol. 3, pp. 422–428, 1997.

[5] H. Saito, I. Ogura, and Y. Sugimoto, "Uniform CW operation of multiple-wavelength vertical-cavity surface-emitting lasers fabricated by mask molecular beam epitaxy," IEEE Photon. Technol. Lett., vol. 8, no. 9, pp. 1118–1120, 1996.

[6] F. Koyama, T. Mukaihara, Y. Hayashi, N. Ohnoki, N. Hatori, and K. Iga, "Two-dimensional multiwavelength surface emitting laser arrays fabricated by nonplanar MOCVD," Electron. Lett., vol. 30, pp. 1947–1948, 1994.

[7] G. G. Ortiz, S. Q. Luong, S. Z. Sun, J. Cheng, H. Q. Hou, G. A. Vawter, and B. E. Hammons, "Monolithic, multiple-wavelength vertical-cavity surface-emitting laser arrays by surface-controlledMOCVD growth rate enhancement and reduction," IEEE Photon. Technol. Lett., vol. 9, pp. 1069–1071, 1997.

[8] Y. Zhou, S. Luong, C. P. Hains, and J. Cheng, "Oxide-confined monolithic, multiple-wavelength vertical-cavity surface-emitting laser arrays with a 40-nm wavelength span," IEEE Photon. Technol. Lett., vol. 10, pp. 1527–1529, 1998.

[9] C. J. Chang-Hasnain, M. W. Maeda, N. G. Stoffel, J. P. Harbison, L. T. Florez, and J. Jewell, “Surface emitting laser arrays with uniformly separated wavelengths,” in Conf. Dig. Int. Semiconductor Laser Conf., Davos, Switzerland, pp. 18–19, 1990.

[10] C. J. Chang-Hasnain, J. P. Harbison, C. E. Zah, M. W. Maeda, L. T. Florez, N. G. Stoffel, and T. P. Lee, “Multiplewavelength tunable surface emitting laser arrays,” IEEE J. Quantum Electron., vol. 27, no. 6, pp. 1368–1376, 1991.

[11] C. J. Chang-Hasnain, C. E. Zah, G. Hasnain, J. P. Harbison, L. T. Florez, and N. G. Stoffel, “Tunable wavelength emission of a 3-mirror vertical cavity surface emitting laser,” in Conf. Dig. Int. Semiconductor Laser Conf., Davos, Switzerland, pp. 24–25, 1990.

[12] C. J. Chang-Hasnain, J. P. Harbison, C. E. Zah, L. T. Florez, and N. C. Andreadakis, “Continuous wavelength tuning of two-electrode vertical cavity surface emitting lasers,” Electron. Lett., vol. 27, no. 11, pp. 1002–1003, 1991.

[13] P. R. Berger, N. K. Dutta, K. D. Choquette, G. Hasnain, and N. Chand, “Monolithic Peltier-cooled vertical-cvity surface-emitting lasers,” Appl. Phys. Lett., vol. 59, no. 1, pp. 117–119, 1991.

[14] L. Fan, M. C.Wu, H. C. Lee, and P. Grodzinski, “10.1 nm range continuous wavelength-tunable vertical-cavity surface-emitting lasers,” Electron. Lett., vol. 30, no. 17, pp. 1409–1410, 1994.

[15] N. Yokouchi, T. Miyamoto, T. Uchida, Y. Inaba, F. Koyama, and K. Iga, “4 angstrom continuous tuning of GaInAsP/InP vertical-cavity surfaceemitting laser using an external cavity mirror,” IEEE Photonics Technol. Lett., vol. 4, no. 7, pp. 701–703, 1992.

[16] C. Gmachi, A. Kock, M. Rosenberger, E. Gormick, M. Micovic, and J. F.Walker,

"Frequency tuning of a double-heterojunction AlGaAs/GaAs vertical-cavity surface-emitting laser by a serial integrated in-cavity modulator diode," Appl. Phys. Lett., vol. 62, pp. 219–221, 1993.

[17] Connie J. Chang-Hasnain, "Tunable VCSEL," IEEE Journal on selected topics in Quantum Electronics, vol. 6, no. 6, 2000.

[18] F. Sugihwo, M. C. Larson, and J. S. Harris, jr, "Simultaneous optimization of membrane reflectance and tuning voltage for tunable vertical cavity lasers," Appl. Phys. Lett., vol. 72, pp. 10–12, 1998.

[19] D. Vakhshoori, J.-H. Zhou, M. Jiang, M. Azimi, K. McCallion, C. C. Liu, K. J. Knopp, J. Cai, P. D. Wang, P. Tayebati, H. Zhu, and P. Chen, "C-band tunable 6mW vertical cavity surface emitting lasere," in Proc. Conf. Optical Fiber Commun., Baltimore, MD, Mar. 2000.

[20] G. Piazza, K. Castelino, A. P. Pisano, and C. J. Chang-Hasnain, "Design of a monolithic piezoelectrically actuated microelectromechanical tunable vertical-cavity surface-emitting laser," Optics Letters, vol. 30, no. 8, 2005.

[21] J. D. Joannopoulos, P. R. Villeneuve and S. Fan, "Photonic crystals: putting a new twist on light," Nature. vol. 386. pp. 143-149, 1997.

[22] K. Sakoda, "Optical Properties of Photonic Crystals," Springer, 2001.

[23] W. Suh and S. Fan, "All-pass transmission or flattop reflection filters using a single photonic crystal slab," Applied Physics Letters. vol. 84. pp. 4905-4907, 2004.

[24] W. Shu and S. Fan, "Mechanically switchable photonic crystal filter with either all-pass transmission or flat-top reflection characteristics," Optics Letters. vol. 28. no. 19. pp. 1763-1765, 2003.

[25] W. Suh, M. F. Yanik, O. Solgaard, and S. Fan, “Displacement-sensitive photonic crystal structures based on guided resonance in photonic crystal slabs,” Applied Physics Letters, vol. 82, no. 13, 2003.

[26] O. Kilic, S. Kim, W. Suh, Y.-A. Peter, M. F. Yanik, S. Fan, and O. Solgaard, “Photonic crystal slabs demonstrating strong broadband suppression of transmission in the presence of disorders,” Optics Letters, vol. 29, no. 23, 2004.

[27] S. Fan and J. D. Joannopoulos, “Analysis of guided resonances in photonic crystal slabs,” Physical Review B, vol. 65, 235112, 2002.

[28] Eric Bisaillon, Dawn Tan, Behnam Faraji, Andrew G. Kirk, Lukas Chrowstowski, and David V. Plant, “High reflectivity air-bridge subwavelength grating reflector and Fabry-Perot cavity in AlGaAs/GaAs,” Optics Express, vol. 14, pp. 2573-2582, 2006.

[29] S. Boutami, B. Ben Bakir, J.-L. Leclercq, X. Letartre, P. Rojo-Romeo, M. Garrigues, P. Viktorovitch, I. Sagnes, L. Legratiet, and M. Strassner, “Highly selective and compact tunable MOEMS photonic crystal Fabry-Perot filter,” Optics Express, vol. 14, pp. 3129-3137, 2006.

[30] M. C. Y. Huang, Y. Zhou and C. J. Chang-Hasnain, “A surface-emitting laser incorporating a high-index-contrast subwavelength grating,” Nature Photonics, vol. 1, pp. 119-122, 2007.

[31] Y. Zhou, et al., “Amplified Stimulated Emission of Sub-Wavelength Gratings Integrated VCSEL," Conf. on Lasers & Electro Optics, CWP6, 2006.

[32] W. Suh, M. F. Yanik, O. Solgaard, and S. Fana, “Displacement-sensitive photonic crystal structures based on guided resonance in photonic crystal slabs,” Applied Physics

Letters, vol. 82, no. 13, 2003.

[33] O. Kilic, S. Kim, W. Suh, Y-A Peter, M. F. Yanik, S. Fan, and O. Solgaard, "Photonic crystal slabs demonstrating strong broadband suppression of transmission in the presence of disorders," Optics Letters, vol. 29, no. 23, 2004.

[34] D.-S. Sung, S.-H. Kim, H.-G. Park, C.-K. Kim, and Y.-H. Lee, "Single fundamental-mode photonic-crystal vertical-cavity surface-emitting lasers," Appl. Phys. Lett., vol. 80, no. 21, pp. 3901–3903, May 2002.

[35] K-H. Lee, et al., "Square-lattice photonic-crystal vertical-cavity surface-emitting lasers," Optics Express, vol. 12, no. 17, 2004.

[36] T. Czyszanowski, M. Dems, and K. Panajotov, "Optimal Parameters of Photonic-Crystal Vertical-Cavity Surface-Emitting Diode Lasers," Lightwave Technology, vol.25, no. 9, 2007.

[37] B. E. A. Saleh and M. C. Teich, "Fundamentals of Photonics," Wiley Interscience, 1991.

[38] G. P. Agrawal, "Fiber-Optic Communication Systems," Wiley Interscience, 2002.

[39] T. P. Pearsall, "Ga0.47In0.53As :A ternary semiconductor for photodetector applications," IEEEJ . Quantum Electron., vol. QE-16. pp. 709-720, 1980.

[40] T. P. Lee, C. A. Burrus, Jr., and A. G. Dentai, "InGaAs/InP p-i-n photodiodes for lightwave communications at the 0.95-1.65 um wavelength," IEEE J. Quantum Electron., vol. QE-17, pp. 232-238, 1981.

[41] K. Kishino, M. S. Unlu, J.-I. Chyi, J . Reed, L. Arsenault, and H. Morkoq, "Resonant Cavity -Enhanced (RCE) Photodetectors," IEEE Journal of Quantum Electronics. vol. 27. no. 8. pp. 2025-2034, 1991.

[42] K. Kishino, M. S. Unlu, J.-I. Chyi, J . Reed, L. Arsenault, and H. Morkoq, "Resonant

Cavity -Enhanced (RCE) Photodetectors," IEEE Journal of Quantum Electronics. vol. 27. no. 8. pp. 2025-2034, 1991.

[43] L. A. Coldren and S. W. Corzine, "Diode Lasers and Photonic Integrated Circuits," Wiley Interscience (1995).

Chapter 2. DBR, Sub-wavelength grating, and Photonic crystal slab Fabry-Perot cavity design using phase analysis by FDTD[1]

2.1. Introduction

A Fabry-Perot (FP) cavity, consisting of two partially transmitting parallel mirrors is a very useful device for filtering specific wavelengths or as a resonator structure for a laser cavity. There are several ways of predicting resonant wavelengths in a FP structure. First, we use the Transfer Matrix Method (TMM) [1]. This Technique is applicable to one-dimensional structures, such as Distributed Bragg Reflectors (DBRs). For higher dimensionality structures, more advanced techniques are necessary, such as Finite-Difference Time-Domain (FDTD). By using the FDTD method, we can obtain a reflectance (or transmittance) from the structure, then determine peaks in the reflectivity plot. However, this technique requires substantial time to run the simulation for accurate results. Also, one may have to run the simulations repeatedly to check the resonant wavelengths if any parameters affecting the resonance are changed (e.g., cavity length). In this regard, a phase analysis would be a good methodology for estimating resonant conditions and providing insight into the FP cavity design process, while reducing simulation time.

In a typical FP resonator, a phase shift imparted by a single roundtrip of the wave propagation is a multiple of 2π [2, 3]. For instance, a total phase response in Fig. 2.1(a) can

---

[1] This chapter has been published in Optics Express, vol.15, pp.10330-10339, 2007.

be expressed as the summation of $\angle\phi_{mirror1}$, $\angle\phi_{cavity}$ $\angle\phi_{mirror2}$, and $\angle\phi_{cavity}$. In this simplified model, the easiest way to shift the resonant wavelength is to vary the cavity length, since this produces the phase shift of the cavity, which changes the resonant wavelength. Therefore, as long as the phase responses of components forming the FP cavity are well known, an exact prediction of resonances is possible in a simple but very effective way. In Fig. 2.1(b), a simplified conventional Vertical-Cavity Surface-Emitting Laser (VCSEL) structure consisting of a top and bottom DBR is shown. Here, the top and bottom DBR are represented as Mirror1 and Mirror2 in Fig. 2.1(a). VCSEL structures are analyzed in detail in the following sections.

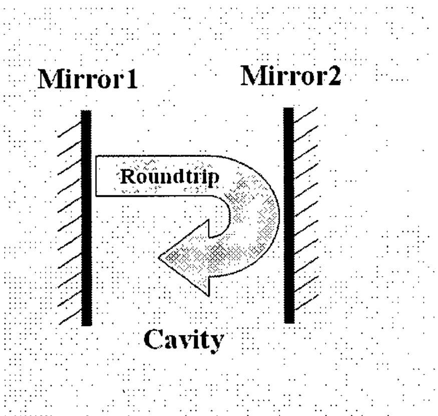

(a)

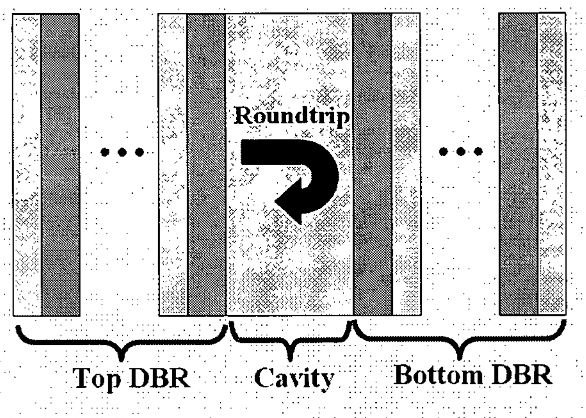

(b)

Fig. 2.1. (a) A simple diagram of a FP cavity assuming for normal incidence. Resonances occur when the roundtrip inside a cavity is a multiple of $2\pi m$ ($m = 0, \pm1, \pm2...$) and (b) a schematic diagram of a simple VCSEL structure forming a FP cavity.

In this paper, we use Lumerical FDTD software for FDTD phase and reflectivity calculations, and Matlab for TMM as well as resonant wavelength predictions based on phase. We start our phase analysis with DBRs and the conventional VCSEL structure, and estimate resonant wavelengths from the total phase response of the VCSEL, using both FDTD phase method and TMM. With the aim of proving our phase analysis to be valid, we compare our results with the FDTD reflectance method. Thereafter, we apply our phase analysis to highly reflective mirrors, such as a Sub-Wavelength Grating (SWG) and a Photonic Crystal (Phc) slab, and discuss how lithographic changes affect reflectivities and phases. We predict resonant conditions after the FP cavity is formed, while varying lithographically defined parameters. In the final section, we investigate maximum tuning ranges for VCSELs, including different types of highly reflective mirrors where corresponding quality factors (cavity Qs) are still above 1,000, by varying them either micromechanically (varying the cavity length) or lithographically (varying lithographic parameters).

2.2. VCSEL structure

The conventional VCSEL structure depicted in Fig. 2.1(b) is a good model for conducting a phase analysis. Here, we set a design wavelength for DBRs to 850nm, and choose the materials $Al_{0.12}Ga_{0.88}As$ (n=3.53) and $Al_{0.9}Ga_{0.1}As$ (n=3.03) to avoid any material absorption at the target wavelength. First, we choose 20 and 27 pairs of alternating $Al_{0.12}Ga_{0.88}As$ and $Al_{0.9}Ga_{0.1}As$ for the top and bottom DBR mirrors, respectively which provide very high reflectivities (99.05% for 20 pairs and 99.9% for 27 pairs in FDTD simulations) at the 850nm wavelength.

For the phase analysis, we use FDTD simulations, where the phase of each DBR is determined by the electric fields being reflected from a single DBR after a TE polarized plane wave is incident to the structure (We use the TE polarized plane wave for all the FDTD simulations).

We vary the cavity length from 100nm to 190nm in 30nm increments, and compare changed resonances using both the FDTD phase and reflectance methods, to make sure that the phase analysis gives an exact prediction. In the phase plot, the resonance is determined at a point where the phase plot intersects at 0. As plotted in Fig. 2.2(a), the total phase moves up or down according to the cavity variation; as a result, the resonant wavelength becomes shorter (phase moving upward) or longer (phase moving downward). In Fig. 2.2(b), FP peaks in the stopband for various cavity lengths are shown. The shifting of those peaks is due to the phase shift demonstrated in Fig. 2.2(a), and shows a good agreement. For L=130nm, the resonant wavelength predicted by FDTD phase and reflectance method is compared with TMM that shows a good agreement within 2nm.

In order to be able to accurately evaluate cavity Q values, the penetration depth of the DBR (l_{eff}) is considered in the calculation. l_{eff} can be calculated by finding 1) a $1/e$ point of the normalized electric field amplitude from the edge of the cavity to the DBR or 2) the mode spacing between resonant frequencies by increasing the cavity length to an integer number of λ. We use method 2) and increase the cavity length to 20λ, which reduces the mode spacing between resonant frequencies in the DBR stopband. The effective cavity length L_{eff} is written as $L_{eff} = L_{cavity} + l_{eff,topDBR} + l_{eff,bottomDBR}$. From the mode spacing (Δv) formula, penetration depths of both DBR pairs are then expressed as $l_{eff,topDBR} + l_{eff,bottomDBR} = \dfrac{c}{2n\Delta v} - L_{cavity}$ (where n = refractive index of the cavity and c = speed of light). Since we use same materials for the top and bottom DBR pairs, l_{eff} can be finally written as $l_{eff} = \frac{1}{2}(\frac{c}{2n\Delta v} - L_{cavity})$. According to our simulations, the penetration depth of the DBR is about 400nm. Therefore, for the VCSEL structure, we can write a formula for the Q calculation as $Q = v_0 \left[\frac{2\{nL_{cavity} + n_{eff,DBR}(l_{eff,topDBR} + l_{eff,bottomDBR})\}}{c} \right] Finesse$ (where v_0 =resonant frequency and $n_{eff,DBR}$ = refractive index of weighted average of DBR materials).

Resonant wavelengths predicted by three different methods over different cavity lengths and corresponding quality factors (cavity Qs), calculated using the formula $Q = \frac{v_0}{\Delta v} Finesse$ (where v_0 =resonant frequency and Δv =mode spacing), are summarized in Table 2.1. A few nm discrepancy might due to the difficulty in resolving the position of the peak precisely. The dispersion relation (w as a function of k) in FDTD is not precisely the same as in real space. This causes small shifts in resonant frequencies.

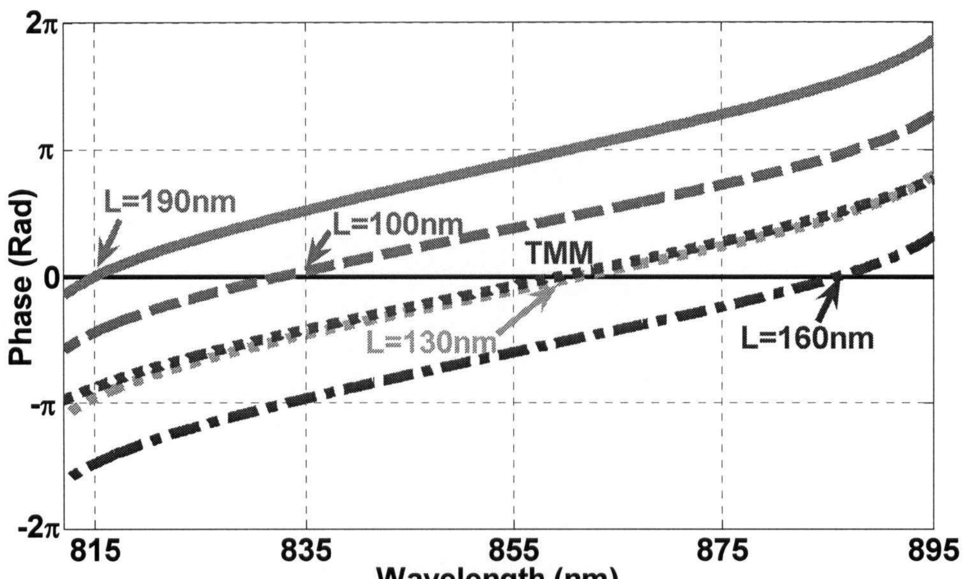

(a)

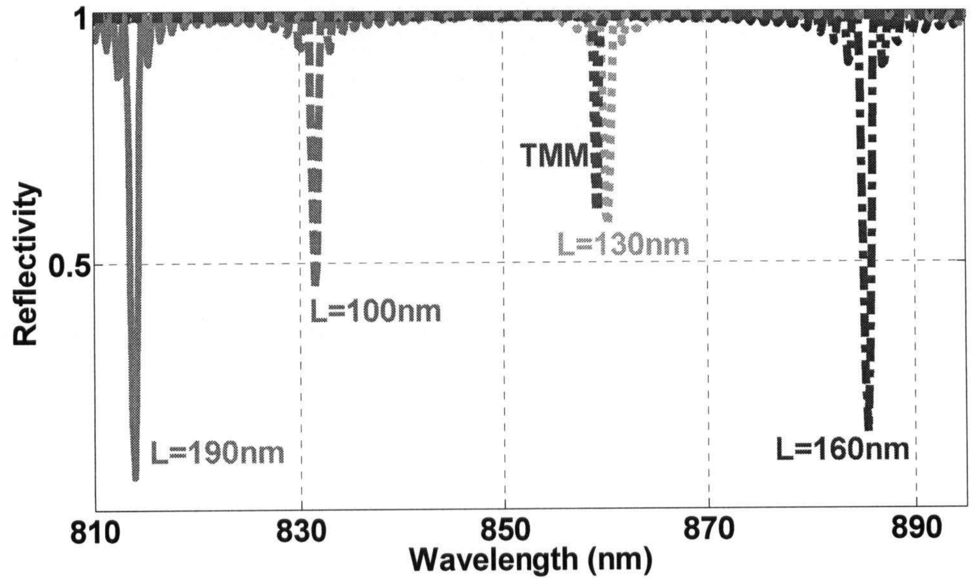

(b)

Fig. 2.2. Resonant wavelengths of the VCSEL structure for various cavity lengths (*L*) estimated by (a) the phase analysis and (b) the notch reflectivity in the DBR stopband.

Table 2.1. Resonant Wavelengths Estimated by Three Different Methods, and Corresponding Cavity Qs.

Cavity Length (nm)	FDTD Reflectance Method (nm)	FDTD Phase Method (nm)	Transfer Matrix Method (nm)	Cavity Q calculated
100	831.6	832.5	830.5	1,855
130	860.3	861.3	859.3	2,231
160	885.2	885.9	884.3	1,241
190	814.6	815.0	813.3	825

2.3. Periodic reflectors

We consider 1-D and 2-D periodic structures, namely a SWG and a Phc slab. High reflectivity can be exhibited from 0th order wave-guide mode grating and the same phenomenon occurs for both structures.

Due to the feasibility of achieving high reflectivities, the SWG is considered to be a device that can replace one of the DBRs in a VCSEL or filter structures [4-6]. Reflectivity mostly depends on how the lithographically defined parameters, i.e., a period (Λ) and a duty factor (α) are set, as well as the thickness of the device. One of the most conspicuous advantages of using the SWG in the VCSEL is that it can vary the effective cavity length lithographically instead of by micromechanically tuning the cavity length, which requires an additional electrostatic force to be operated [7]. Also, by replacing a DBR a few micrometers thick (e.g., ~4um for 30 pairs intended for a 850nm wavelength) with a device that is hundreds of nanometers thick (e.g., ~250nm thick SWG or Phc slab in our design), it is possible to achieve a more compact-sized structure [4, 5].

Phc slabs provide unique characteristics in terms of supporting guided resonances whose electro-magnetic power is strongly confined within the slab, as well as in-plane guided modes that are completely confined by the slab without any coupling to external radiation [8]. A not very well-exploited property of Phc slabs is that a relatively wide range of high reflectivities is possible by appropriate settings of lithographic parameters such as the slab thickness, the square lattice constant (a) and the radius of the air hole (r) [8-10]. Similar to the SWG, Phc slabs are very useful for changing the effective cavity length lithographically rather than by micromechanical tuning.

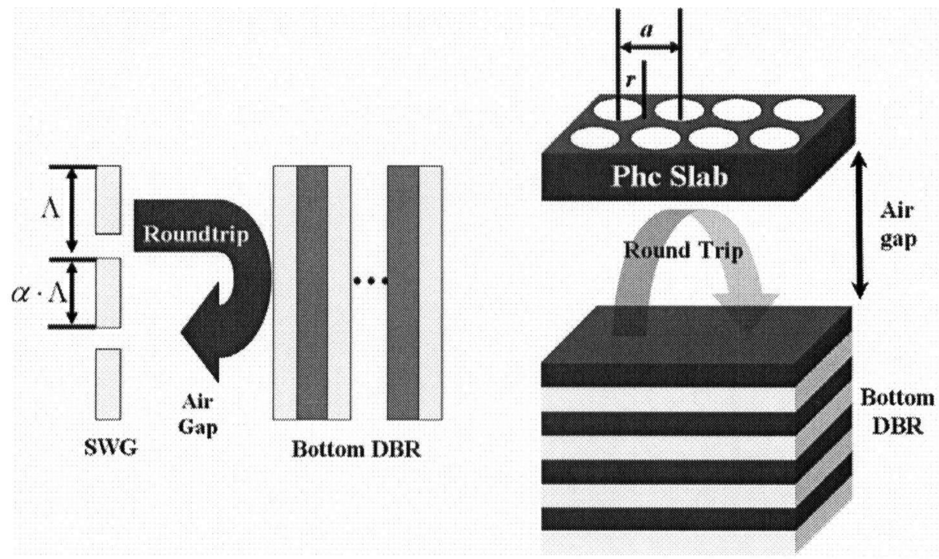

(a) (b)

Fig. 2.3. The schematic diagram of two VCSEL structures, consisting of the air gap, 27.5 DBR pairs, and (a) the SWG and (b) the Phc slab forming the FP cavity.

2.3.1 Sub-wavelength grating

In this section, we examine the reflectivities and phases of a single SWG as a function of Λ and α and resonant conditions of the VCSEL, with the SWG used as a top mirror and 27.5 bottom DBR pairs. We choose $Al_{0.12}Ga_{0.88}As$ for the SWG slab and set design parameters to $\Lambda = 420$nm, $\alpha \cdot \Lambda = 310$nm ($\alpha$ =0.738), and the thickness of the SWG to 163nm, so that high reflectivities are placed at the design wavelength. In Fig. 2.3(a), definitions of Λ and α in the SWG (assuming air-suspended), as well as a schematic diagram of the VCSEL incorporating the SWG, the cavity, and 27.5 DBR pairs are shown. As a consequence of using the 163nm thick SWG instead of 20 pairs of 2.6um thick DBR, the resonator is far smaller.

For the cavity design, we set the air gap to 860nm, in order that the resonant peak occurs at the target wavelength. The air gap plays an important role in providing a high refractive index contrast for the SWG. Sacrificial etch relaxes the etching tolerance and leaves a smooth surface in fabrication [4].

We determine the reflectivities and phases of a single SWG while varying the lithographic parameters. In Fig. 2.4, the duty factor (α) is first changed to 0.643, 0.690, and 0.738 (plots A, B, and C, respectively), while the period (Λ) is fixed at 420nm. Then, Λ is adjusted to 420nm, 440nm, and 460nm (plots C, D, and E, respectively), while α is set to 0.738. In other words, the plots A→C and C→E show effects of α and Λ on reflectivities and phases. With increasing α or Λ, not only do peak reflectivities tend to shift to longer wavelengths (Fig. 2.4(a)), but phases are apt to move in a downward direction (Fig. 2.4(b)). Based on these results, it is clear that varying the SWG lithographic parameters α or Λ can produce the phase shift.

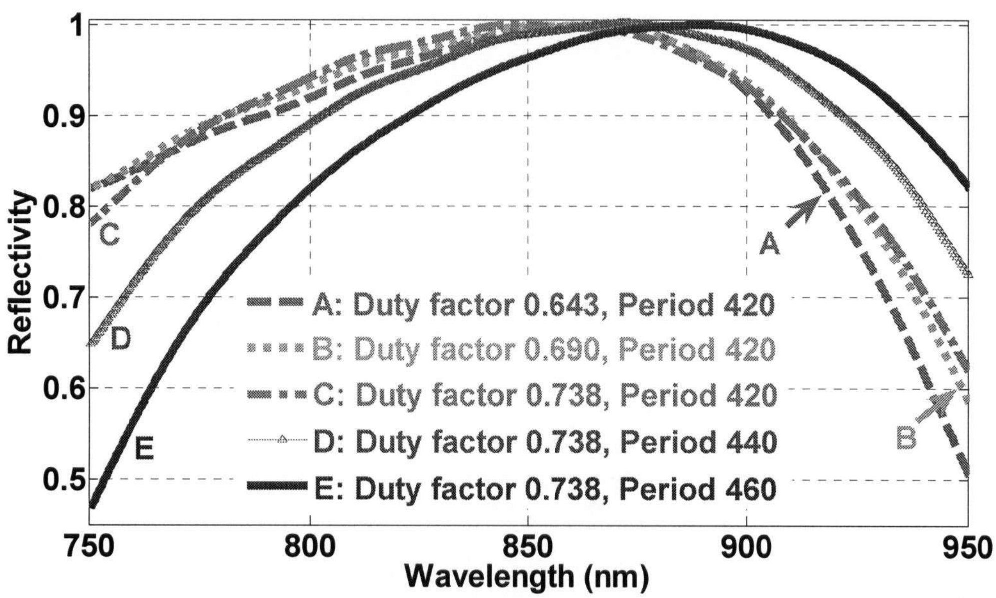

(a)

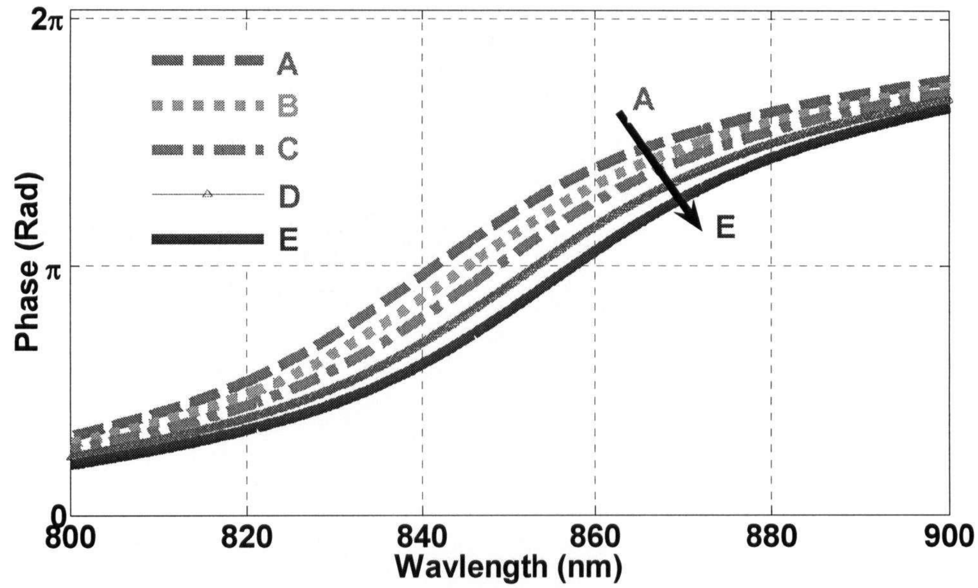

(b)

Fig. 2.4. (a) Reflectivities and (b) phases of a single SWG as varying the duty factor (A→C) and the period (C→E).

In Fig. 2.5(a), we determine phases of the SWG VCSEL shown in Fig. 2.3(a) and estimate resonant wavelengths from phase plots. The total phase response of the SWG VCSEL is the sum of an individual phase of the SWG, the cavity (air gap), and 27.5 DBR pairs. Resonances can be predicted by measuring specific points where phase plots intersect at 0. By increasing either α (A→C) or Λ (C→E), the phase plot tends to move in a downward direction, which results in a longer resonant wavelength. FP peaks in the stopband are shown in Fig. 2.5(b), and are in good agreement with the resonances shown in Fig. 2.5(a). Table 2.2 summarizes resonant wavelengths estimated by the FDTD phase and reflectance methods, and corresponding cavity Qs, using the formula introduced in the previous section. l_{eff} is determined with the same method used for the conventional VCSEL case. According to our FDTD simulations, the penetration depth of the SWG is about 386nm. The maximum discrepancy between the two methods is less than 1nm.

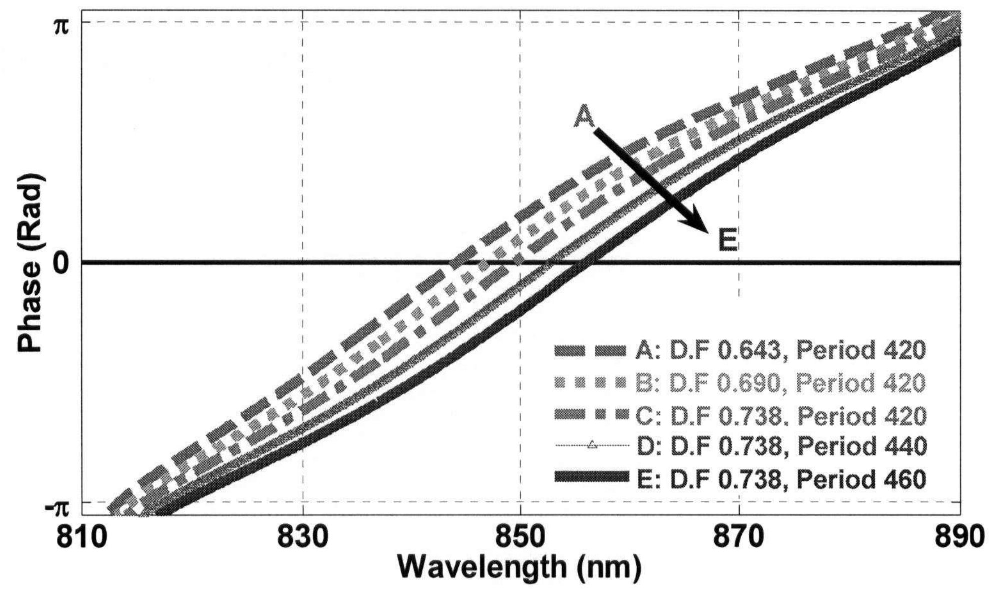

(a)

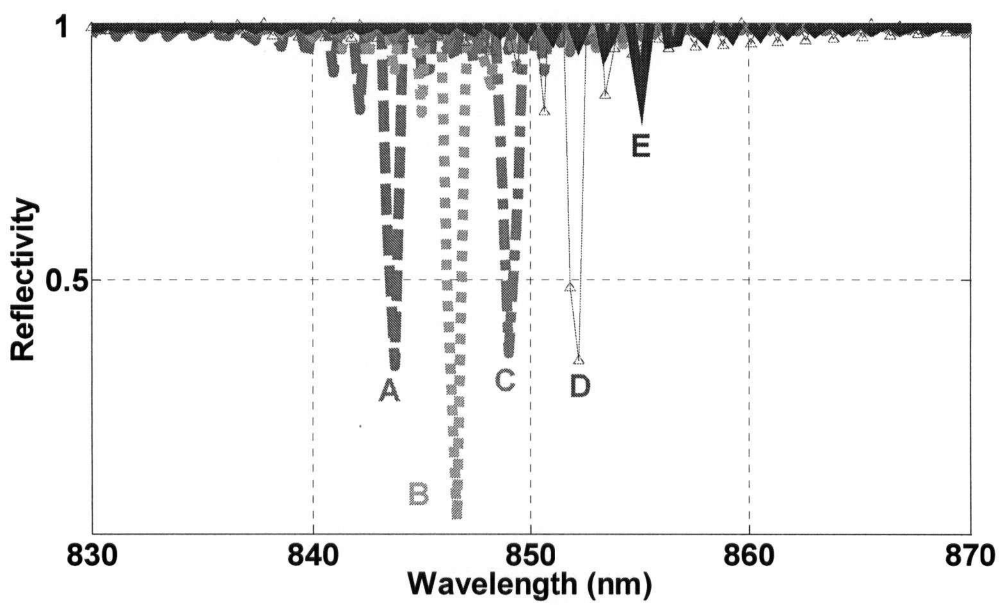

(b)

Fig. 2.5. (a) Phase responses of the SWG VCSEL and (b) resonant wavelengths shown in the

DBR stopband as the duty factor (A→C) and the period (C→E) are varied.

Table 2.2. Resonant Wavelengths Estimated by Two Different Methods, and Corresponding Cavity Qs.

Plot	α	Λ	**FDTD Phase Method (nm)**	**FDTD Reflectance Method (nm)**	**Cavity Q calculated**
A	0.643	420	844.2	843.8	2,247
B	0.690	420	847.0	846.5	4,703
C	0.738	420	849.5	849.0	17,057
D	0.738	440	852.9	852.2	2,521
E	0.738	460	856.1	855.1	904

2.3.2 Photonic crystal slab

We select the $Al_{0.12}Ga_{0.88}As$ for the Phc slab material and set the slab thickness, the square lattice constant, and the radius of the air hole to 230nm, 446nm, and 0.48*a*, respectively, so that high reflectivities lie on the design wavelength.

In Fig. 2.3(b), definitions of *a* and *r* in a square lattice Phc slab, as well as a schematic diagram of the VCSEL incorporating the Phc slab as a top mirror, the cavity, and 27.5 bottom DBR pairs, are shown. For the cavity design, we set the air gap to 800nm, so that the resonant peak occurs at the design wavelength. The 800nm thick air gap and 27.5 bottom DBR pairs are used for the same reasons they were in the SWG VCSEL, described earlier.

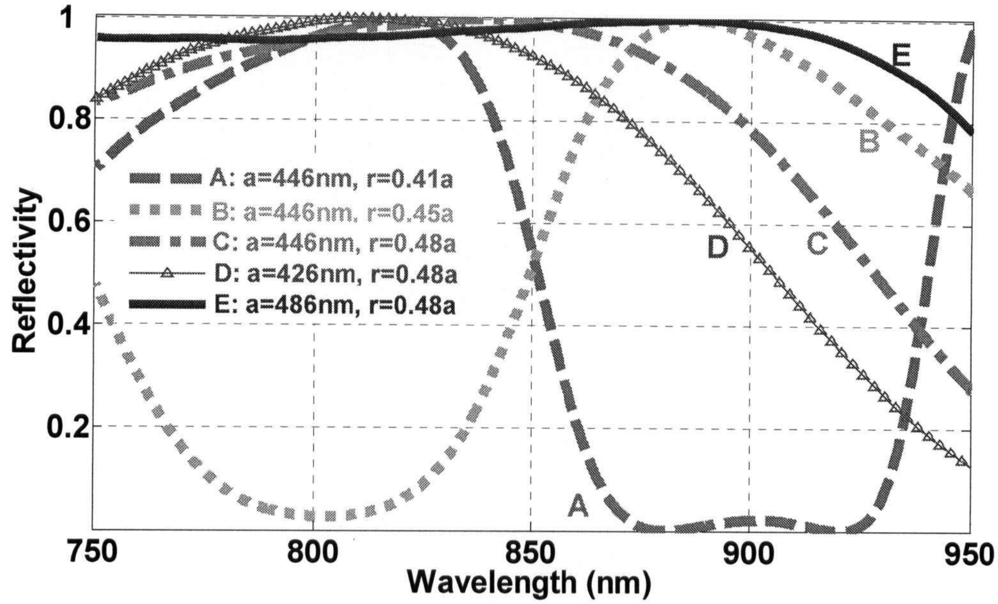

(a)

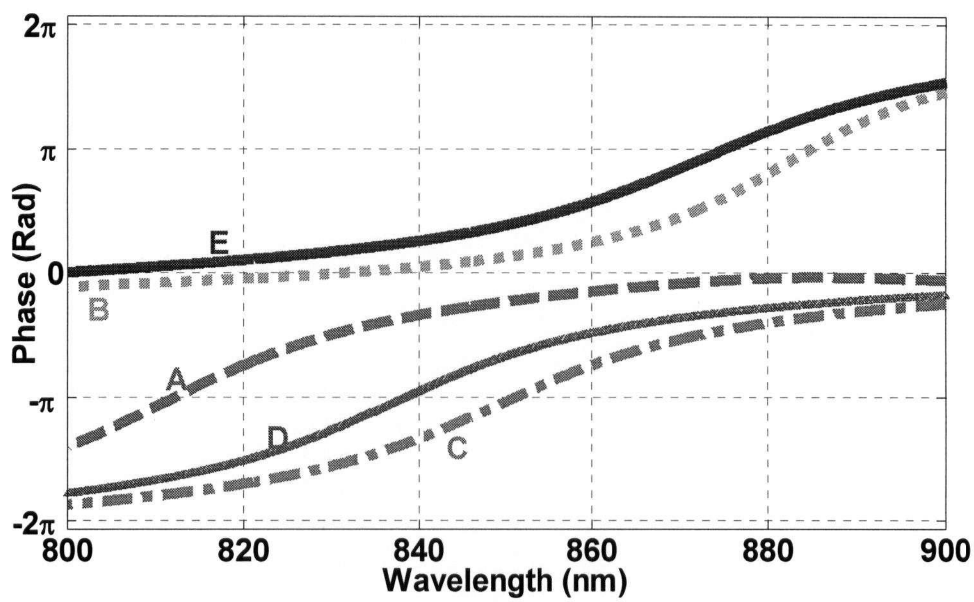

(b)

Fig. 2.6. (a) Reflectivities and (b) phases of a single Phc slab as the radius of the air hole is adjusted (A→B→C), and the lattice constant is varied (D→C→E).

We determine reflectivities and phases of a single Phc slab under varying lithographic parameters. In Fig. 2.6, the radius of the air hole (r) is first changed to $0.41a$, $0.45a$, and $0.48a$ (plots A, B, and C, respectively), while the lattice constant (a) is fixed at 446nm. Then, a is changed to 446nm, 426nm, and 486nm (plots C, D, and E, respectively), while r is set to $0.48a$. In Fig. 2.6(a), two high reflectivity peaks of plot A at around 820nm and 950nm are conspicuous, and tend to move to shorter wavelengths with increasing r. In other words, the high reflectivity peaks of plots B (at 880nm) and C (at 850nm) originate with the second high peak of plot A. It is interesting that as r is increased, the high reflectivity span becomes broader. As well, as a is increased, not only do the high reflectivity peaks tend to shift to longer wavelengths (D→C→E), but also the high reflectivity span becomes wider. Very large air holes are more useful in terms of obtaining high reflectivities in a relatively wider wavelength range than are smaller holes due to the decreased lifetimes of guided resonances [9,10], but care should be taken in fabrication since adjacent holes are more likely to be connected with each other during e-beam lithography. In Fig. 2.6(b), the phase response of the Phc slab reflects the changes in lithographic parameters, with either a or r giving rise to the phase shift.

In Fig. 2.7(a), the phases of the Phc VCSEL (shown in Fig. 2.3(b)) over the stopband are plotted. Resonances can be predicted by measuring the intersections between each phase and the -2π, 0, and 2π lines. The effect of increasing r to $0.41a$, $0.45a$, and $0.48a$ (A→B→C, respectively) is to shift the phase plot upward (plot C appears below plot B due to a -2π phase shift). Also, increasing a to 426nm, 446nm, and 486nm (D→C→E, respectively), shifts the phase plot downward (plot E is shown above plot D owing to a 2π phase shift).

FP peaks in the stopband are shown in Fig. 2.7(b), and the results are in a good agreement with the phase analysis. Table 2.3 summarizes the resonant wavelengths estimated by FDTD phase and reflectance methods and the corresponding cavity Qs. According to our FDTD simulations, the penetration depth of the Phc slab is about 949nm. The maximum discrepancy between the two methods is less than 1.5nm.

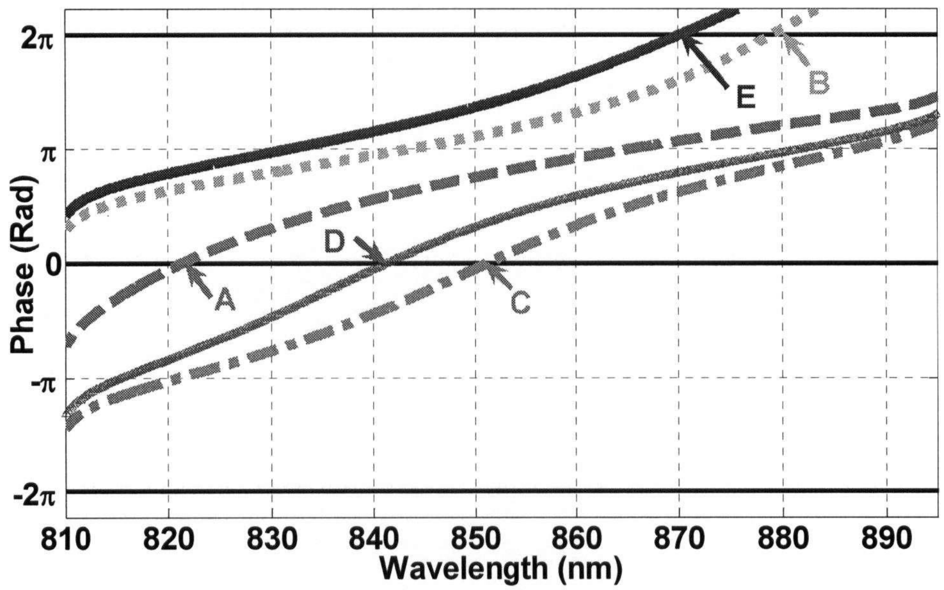

(a)

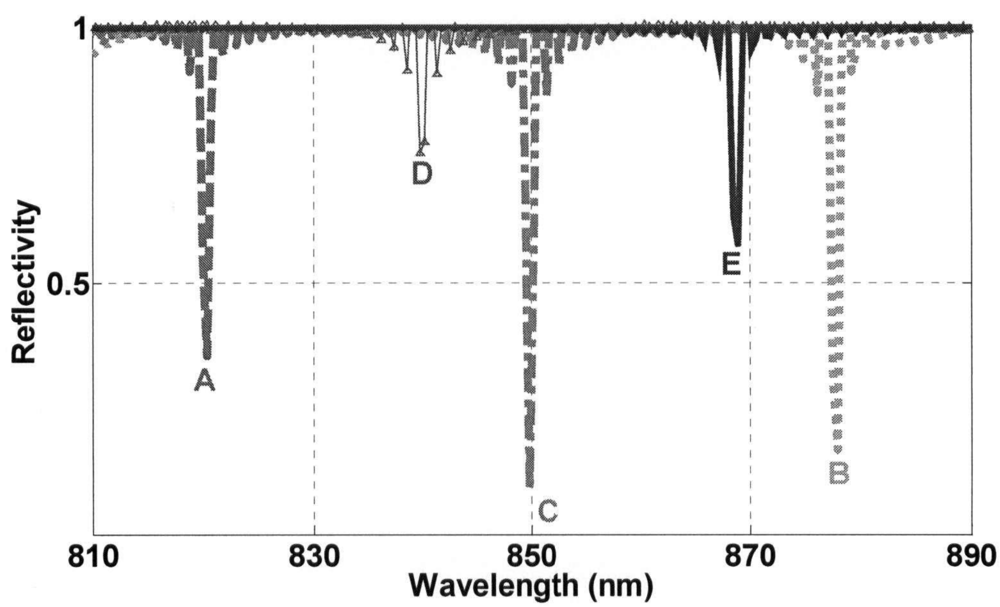

(b)

Fig. 2.7. (a) Phase responses of the Phc VCSEL and (b) resonant wavelengths shown in the stopband under varying r (A→B→C) and a (D→C→E).

Table 2.3. Resonant Wavelengths Estimated by Two Different Methods, and Corresponding Cavity Qs.

Plot	*a* *(nm)*	*r*	FDTD Phase Method (nm)	FDTD Reflectance Method (nm)	Cavity Q calculated
A	446	0.41*a*	821.4	820.4	12,090
B	446	0.45*a*	879.1	877.9	1,397
C	446	0.48*a*	851.2	849.8	4,354
D	426	0.48*a*	841.3	840.0	778
E	486	0.48*a*	870.1	868.9	6,225

2.4. Resonance tunability

In this section, we study maximum tunability and the corresponding cavity Qs for the three different VCSEL structures demonstrated previously. Resonance tuning is done by varying either the cavity or lithographic parameters; here, both methods are considered. Since we assume that cavity tuning is performed by varying the air gap between two mirrors, the air gap and is considered as the cavity for the conventional VCSEL structure shown in Fig. 2.1(b). Detailed design factors are summarized in Table 2.4.

Table 2.4. Three different VCSEL structures aimed at the 850nm resonant wavelength.

<table>
<tr><th>Plot</th><th>Structure</th><th>Mirror 1</th><th>Mirror 2</th><th>Cavity</th></tr>
<tr><td>A</td><td>Conventional VCSEL</td><td>20.5 Pairs DBR</td><td rowspan="3">27.5 pairs DBR</td><td>423nm Air gap</td></tr>
<tr><td>B</td><td>SWG VCSEL</td><td>163nm thick SWG (α =0.738, Λ =420nm)</td><td>860nm Air gap</td></tr>
<tr><td>C</td><td>Phc VCSEL</td><td>230nm thick Phc slab (*a*=446nm, *r*=0.48a)</td><td>800nm Air gap</td></tr>
</table>

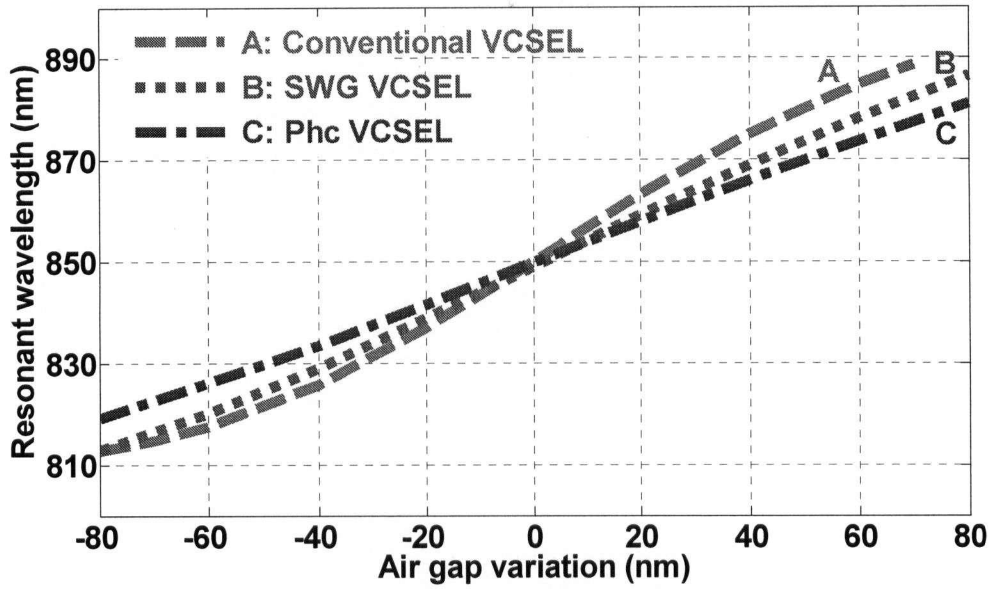

(a)

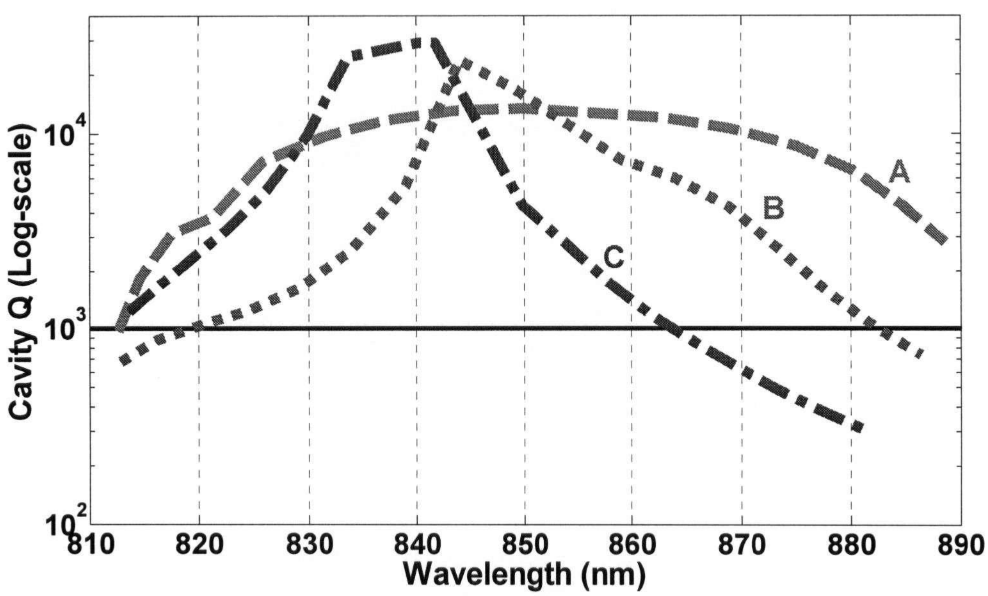

(b)

Fig. 2.8. (a) Tuning slopes of the three different VCSEL structures according to air gap variation in the cavity and (b) corresponding cavity Qs at resonances.

First, we adjust the air gap from the designed cavity (air gap variation=0) for each structure in order to demonstrate their respective tuning sensitivities as shown in Fig. 2.8(a). The conventional VCSEL has the steepest tuning slope, representing the best micromechanical tunabililty, followed by the SWG VCSEL and the Phc VCSEL. In Fig. 2.8(b), the cavity Qs at resonances and maximum tunable ranges where Q values are higher than 1,000 are shown. The conventional VCSEL has the widest tunable range due to the high reflectivity plateau over the stopband, whereas the SWG VCSEL and Phc VCSEL provide limited ranges of high reflectivity of 61nm (820nm~881nm) and 48nm (815nm~863nm), respectively, as shown in Fig. 2.4(a) and Fig. 2.6(a).

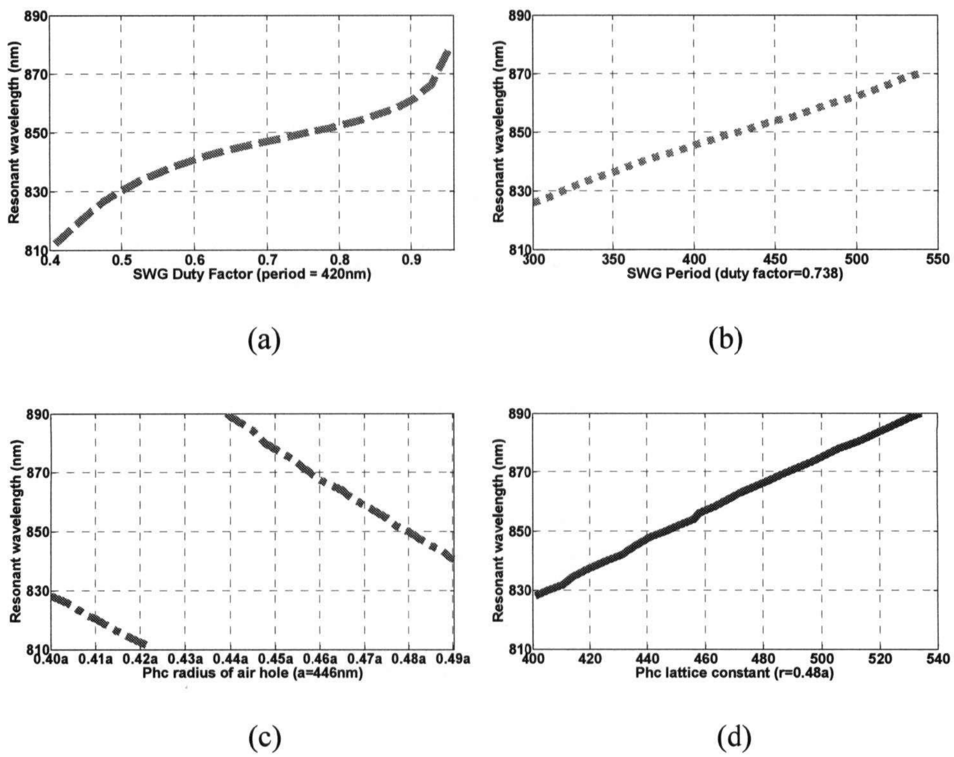

Fig. 2.9. Resonance tuning by (a) SWG duty factor (α), (b) SWG period (Λ), (c) Phc radius of the air hole (r) and (d) Phc lattice constant (a).

Finally, we demonstrate resonance tuning by varying lithographic parameters for the

SWG and Phc VCSELs on resonance tuning in Fig. 2.9(a) ~ (d), and the maximum tunable ranges (Q >1,000) lithographically achievable in Fig. 2.10. The shifting of resonant wavelengths is due to an effective refractive index change on the in-plane slab where lithographic parameters are varied. The results show that the tunable ranges achieved by varying α (SWG) and r (Phc slab) are approximately 60nm (817nm~877nm) and 61nm (813nm~824nm and 830nm~880nm), respectively. As well, resonance tuning by Λ (SWG) and a (Phc slab) is only possible in a relatively limited range for each, 14nm (SWG VCSEL) and 49nm (Phc VCSEL), respectively, which suggests that α and r are more effective than Λ and a for lithographic resonance tuning in VCSEL structures.

It is also interesting to note that for both SWG and Phc designs, there are two parameters that can be varied: this allows one to change both parameters to fine tune both the resonant frequency as well as the cavity Q, providing more flexibility in the design.

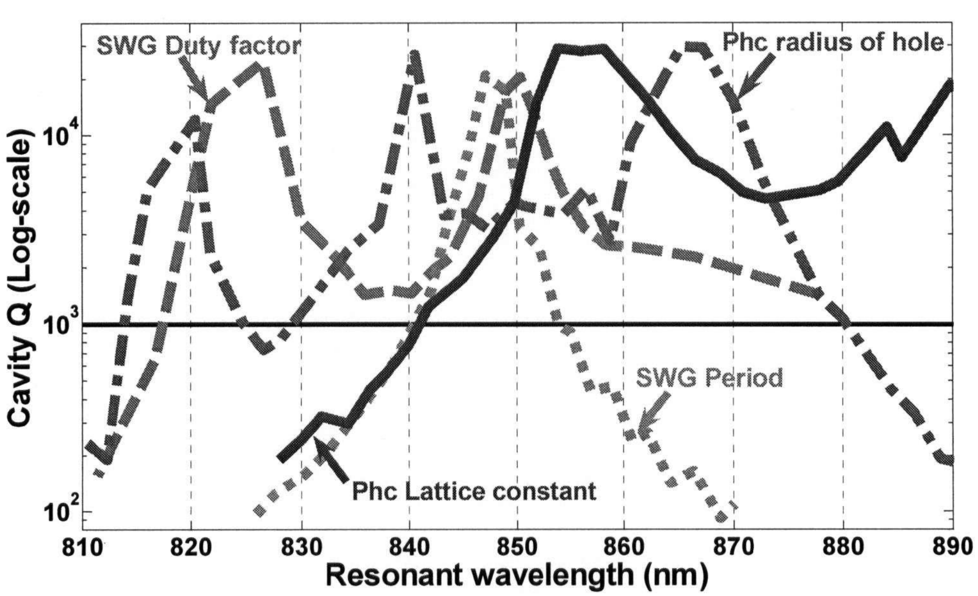

Fig. 2.10. Cavity Qs at resonances for the SWG and Phc VCSEL, lithographically (α, Λ, r, a) tuned.

2.5. Cavity design for a Phc VCSEL

In this section, two different cavity designs for the Phc VCSEL are compared, focusing on resonant tunabilities where cavity Qs are taken into consideration. When using the same materials for the Phc slab and the DBR pairs in the Phc VCSEL, intended for the 850nm resonant wavelength as shown in Section 2.3.2, we can place a 130nm thick $Al_{0.12}Ga_{0.88}As$ and 480nm thick air gap above the 27 bottom DBR pairs, similar to the SWG VCSEL in [4]. This design was presented at a conference [11], and subsequently improved upon.

The other way to form the cavity is to put the 800nm thick air gap above 27.5 bottom DBR pairs, demonstrated in Fig. 2.3(b). In other words, instead of using a relatively thicker $Al_{0.12}Ga_{0.88}As$ layer, we can place one more high refractive index layer into DBR pairs (i.e., 27.5 pairs), while increasing the thickness of the air gap so that the design wavelength occurs at the 850nm. Here, for comparison, we define the first and second cavity type as DESIGN1 and DESIGN2, respectively. The schematics of the two cavity designs are shown in Fig. 2.11.

First, we examine the resonant tunabilities for two different VCSEL structures by varying either a or r. For the r variation, we set the a to 446nm and change the r from $0.40a$ to $0.49a$. Similarly, for the a variation, the a is varied from 400nm to 600nm, while the r is fixed to $0.48a$. As shown in Fig. 2.12(a) and (b), it is very obvious that DESIGN2 provides wider tuning ranges than DESIGN1 in both r and a variation, i.e., produces steeper tuning slopes.

In Fig. 2.13, we look into the maximum tunabilities for two cavity designs while considering cavity Qs (Q>1,000). In Fig. 2.12(a), for the r variation, the tunable range for the DESIGN2 is about 61nm (813nm ~ 824nm and 830nm ~ 880nm), while DESIGN1 only provides 28nm (830nm ~ 858nm). As well, for the a change, DESIGN2 gives approximately 49nm tuning range (841nm ~ 890nm), while 21nm (846nm ~ 867nm) is expected from DESIGN1.

To sum up, judging from the comparison results, it is more effective to put air gap above the 27.5 bottom DBR pairs (DESIGN2), rather than placing the spacer and the air gap into the 27 bottom DBR pairs (DESIGN1), to achieve wider lithographic tuning ranges where cavity Qs are still high.

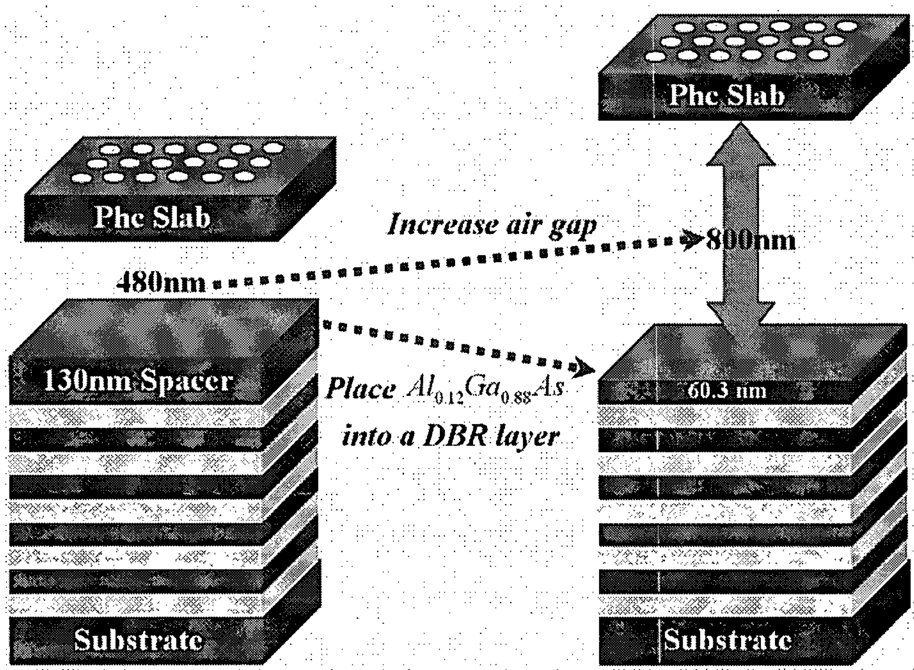

(a) (b)

Fig. 2.11. (a) The Phc VCSEL including a 130nm $Al_{0.12}Ga_{0.88}As$ spacer and a 480nm air gap as a cavity (DESIGN1), and (b) the 800nm air gap placed above 27.5 bottom DBR pairs for the cavity (DESIGN2).

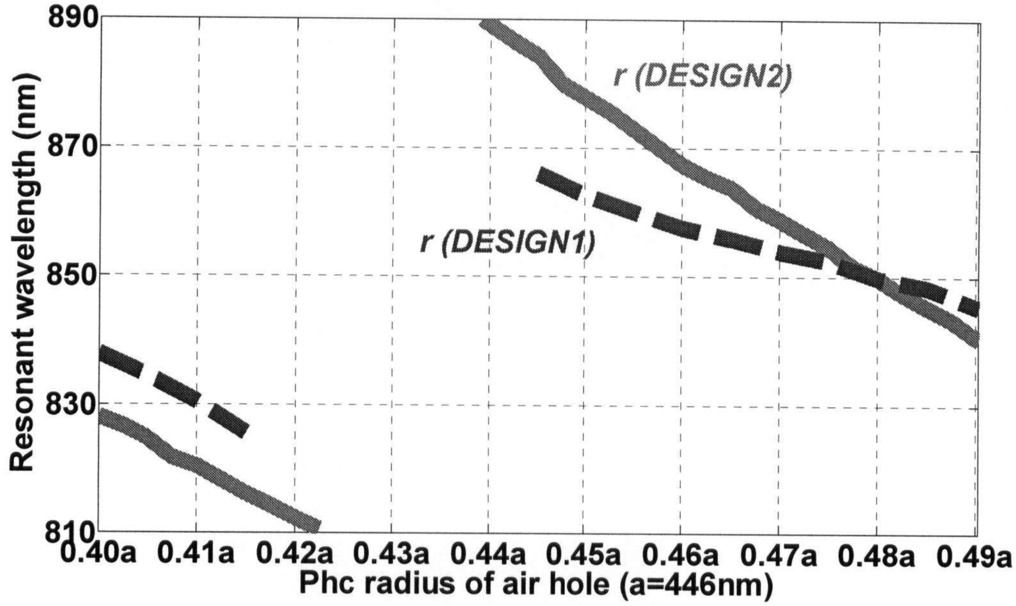

(a)

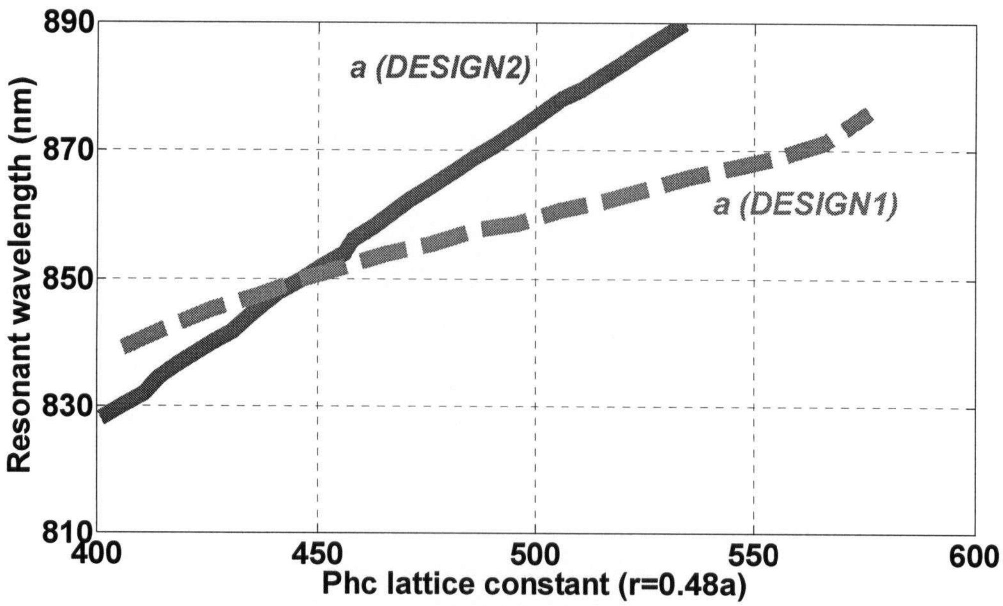

(b)

Fig. 2.12. Resonance tuning of two cavity designs by (a) varying r (a=446nm) and (b) changing a (r=0.48a).

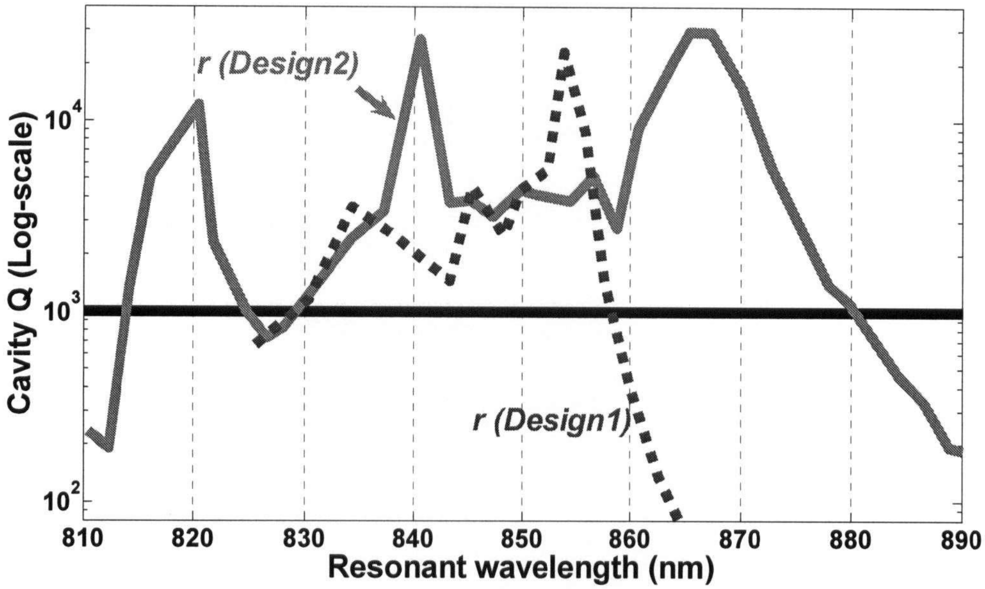

(a)

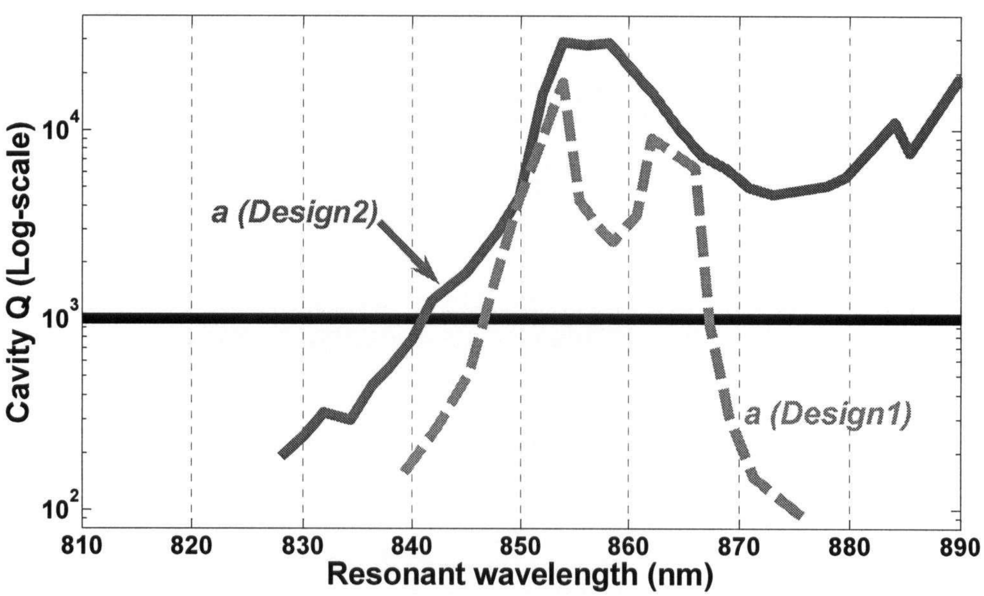

(b)

Fig. 2.13. Cavity Qs of two cavity designs at resonances by (a) varying r (a=446nm) and (b) changing a (r=0.48a).

2.6. Conclusion

We have presented a phase methodology to determine the phase of a single DBR, SWG, and Phc slab to be used as one of the mirrors in the VCSEL, and have estimated resonant wavelengths for the three different VCSEL structures. The maximum discrepancy between the FDTD phase and reflectance method was found to be less than 1.5nm throughout the simulations, indicating that our phase analysis is effective in accurately predicting resonances. The tunable range of the conventional VCSEL by adjustment of the cavity length was found to be about 76nm, compared to only 61nm and 48nm for SWG and Phc MEMS VCSEL.

Varying lithographically defined parameters, in particular, α (SWG) and r (Phc slab) allows for designing multi-wavelength arrays that can provide wide resonance tunability, which do not require a tuning voltage. We demonstrate that lithographical resonance tuning can be achieved up to a range of 60nm (SWG VCSEL) and 87nm (Phc VCSEL), while maintaining relatively high cavity Q values (>1,000). Phase and reflectivity peak are coincident for a broad range of FP wavelengths, resulting in a high cavity Q over a broad tuning range. This is a major improvement compared to the previous work in FP cavities in SWG [4].

References

[1] L. A. Coldren and S. W. Corzine, "Diode Lasers and Photonic Integrated Circuits," Wiley Interscience (1995).

[2] B. E. A. Saleh and M. C. Teich, "Fundamentals of Photonics," Wiley Interscience (1991).

[3] A. Yariv, "Optical Electronics in Modern Communications," Oxford University Press (1997).

[4] E. Bisaillon, D. Tan, B. Faraji, A. G. Kirk, L. Chrowstowski, and D. V. Plant, "High reflectivity air-bridge subwavelength grating reflector and Fabry-Perot cavity in AlGaAs/GaAs," Optics Express. **14**, 2573-2582 (2006).

[5] S. Boutami, B. B. Bakir, J.-L. Leclercq, X. Letartre, P. Rojo-Romeo, M. Garrigues, P. Viktorovitch, I. Sagnes, L. Legratiet, and M. Strassner, "Highly selective and compact tunable MOEMS photonic crystal Fabry-Perot filter," Optics Express. **14**, 3129-3137 (2006).

[6] M. C. Y. Huang, Y. Zhou and C. J. Chang-Hasnain, "A surface-emitting laser incorporating a high-index-contrast subwavelength grating," Nature Photonics. **1**, 119-122 (2007).

[7] C. J. Chang-Hasnain, "Tunable VCSEL," IEEE Journal on selected topics in Quantum Electronics. **6**, 978-987 (2000).

[8] S. Fan and J. D. Joannopoulos, "Analysis of guided resonances in photonic crystal slabs," Physical Review. B **65**, 235112 (2002).

[9] W. Suh, M. F. Yanik, O. Solgaard, and S. Fana, "Displacement-sensitive photonic crystal structures based on guided resonance in photonic crystal slabs," Applied Physics Letters. **82**, 1999-2001 (2003).

[10] O. Kilic, S. Kim, W. Suh, Y.-A. Peter, A. S. Sudbø, M. F. Yanik, S. Fan, and O. Solgaard, "Photonic Crystal slabs demonstrating strong broadband suppression of transmission in the presence of disorders," Optics Letters. **29**, 2782-2784 (2004).

[11] J. Kim and L. Chrostowski, "Fabry-Perot Cavity Design in AlGaAs/GaAs using a Photonic Crystal Slab for a Resonant Cavity Detector," LEOS Conference proceeding, 2006.

Chapter 3. Device fabrication

3.1. Wafer specification

The wafer specification we fabricate is shown in Fig. 3.1(a). We use a 230nm thick $Al_{0.12}Ga_{0.88}As$ for the Phc slab, a 480nm thick $Al_{0.9}Ga_{0.1}As$ for the sacrificial layer, a 130nm thick $Al_{0.12}Ga_{0.88}As$ for a spacer layer, and 30 $Al_{0.12}Ga_{0.88}As$ / $Al_{0.9}Ga_{0.1}As$ DBR pairs. This wafer is based on Design 1 shown in Fig. 2.11 and described in section 2.5.

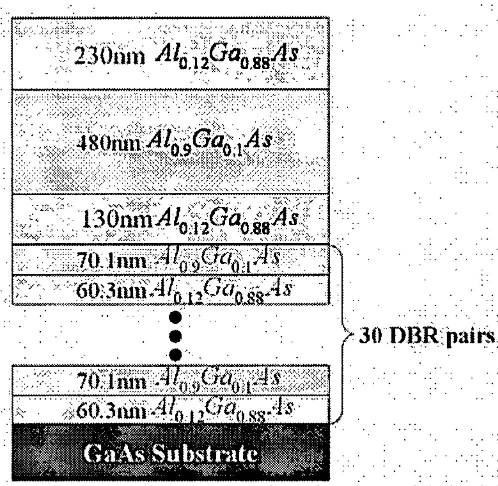

Fig. 3.1. A schematic of the wafer for a Phc FP structure, based on Design 1 in Section 2.5.

3.2. Pattern writing on GaAs slab

Here, photonic crystal arrays are written on the GaAs slab by either using a Focused Ion Beam (FIB) or e-beam lithography, followed by dry-etching.

FIB transfers patterns to a wafer by direct drilling using the gallium ion beam without application of a masking material, which enables users to operate the machine very easily. As well, SEM imaging is available immediately after milling, which is very convenient and helpful for users to check patterns in real time and optimize the equipment settings and parameters [1-3].

To progress e-beam lithography, photoresist should be deposited on the surface of a wafer. However, spinning usually results in non-uniform deposition of the photoresist; i.e., different thickness at the center versus edges may deteriorate the e-beam focusing. In addition, if the etch rate of the resist mask over the substrate to be dry etched is considerable, sidewalls of the patterns could be a concern. In this respect, FIB would be helpful to obtain uniform patterns, since there is no requirement for photoresist spinning.

On the other hand, fabrications of 2D photonic crystals or sub-wavelength gratings have been widely implemented using e-beam lithography in Scanning Electron Microscope (SEM), followed by dry-etching in ECR or RIE, which is considered to be a conventional way of making patterns on the substrate [4, 5]. One of the most crucial benefits of using this method is that it prevents a surface being damaged during patterning, and results in high-quality patterns.

3.2.1. Focused Ion Beam (FIB)

We set the acceleration voltage and beam current of the FEI Strata Dualbeam SEM/FIB to 30KV and 30pA, respectively, while varying the dwell time and the number of milling points to control the shapes of patterns and the drilling depth. Stream files to be loaded to the FIB are made by Matlab. A hole is designed by placing several small points inside and then set in the array, as shown in Fig. 3.2.

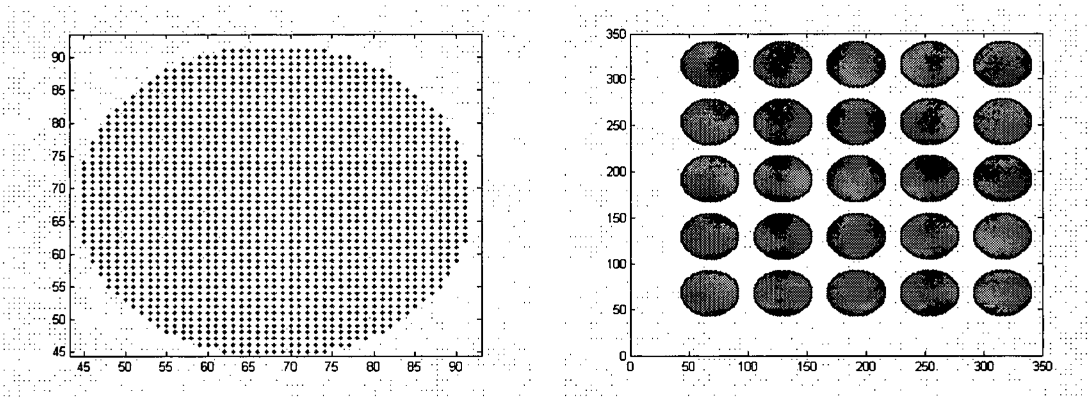

Fig. 3.2. (a) Formation of a single hole by putting small dots inside and (b) 5 X 5 array design.

Fig. 3.3 shows SEM images after our first trial of the FIB milling for a square lattice (a=446nm) of 170nm radius air holes with 1.5 microseconds dwell time. However, we found that the holes could not be made completely due to insufficient milling. We suspect that redeposition of the milled material results in a closing of the holes. The shapes of the holes and the milling depth are also measured by Atomic Force Microscopy (AFM) in Fig. 3.4. The scanning by AFM shows that the holes are elliptical and are approximately 50nm in depth; they should be deeper than 230nm, at a minimum.

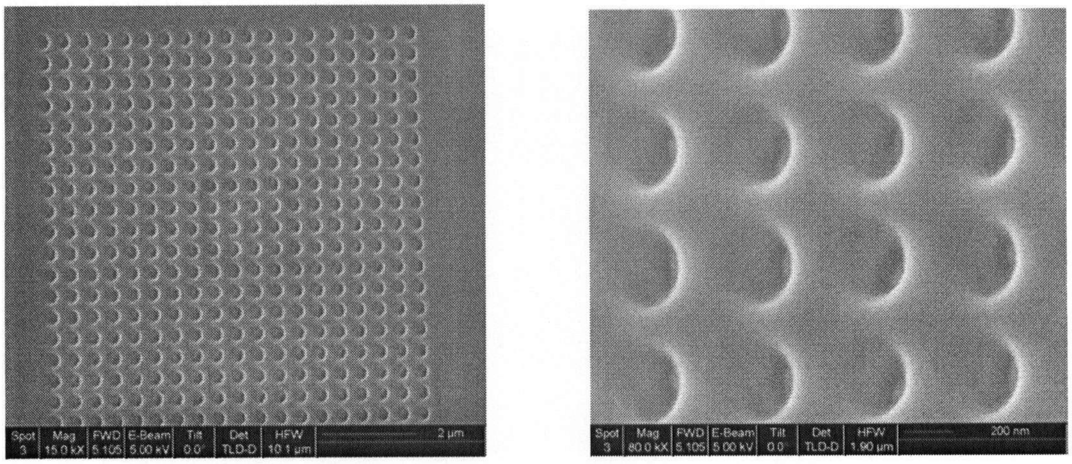

(a) (b)

Fig. 3.3. (a) First trial of writing square-lattice (a=446nm and r=170nm) photonic crystal patterns with a 1.5microseconds dwell time and (b) zoom-in of the holes.

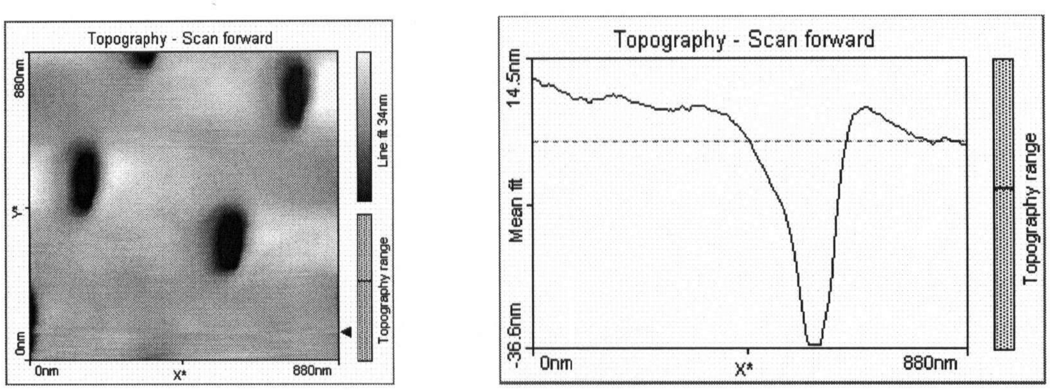

(a) (b)

Fig. 3.4. (a) Surface scanning of the patterns and (b) etching depth of a hole using AFM.

To improve the quality of patterns, we modified the stream files so that every side of the hole can be entirely drilled; i.e., as shown in Fig. 3.5, for a single hole, drilling is performed in sequence from (1) to (4) (up→down, down→up, left→right, then right→left). Thus, the beam passes the same etching area multiple times and redeposition is minimized. This is a known problem and the new RAITH FIB machine can do this automatically.

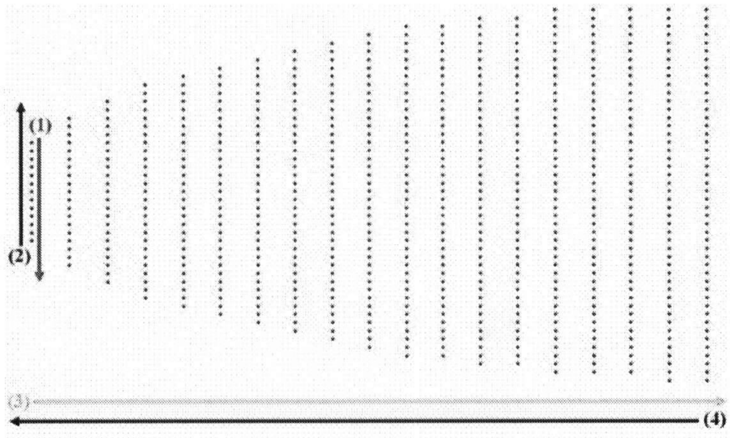

Fig. 3.5. Drilling is repeated as an addition of sequences (1)→(4).

Fig. 3.6 shows SEM images of holes by varying the dwell time and the number of loop (for example, 5 loops mean every hole is milled 5 times) after milling. With regard to the quality of the holes, after implementation of the sequences in Fig. 3.5, it is obvious that the holes are well made. As well, we see that when the dwell time is too excessive, here 1.5 microseconds, holes might be substantially deformed with blurry edges, resulting from the reaction between the gallium ion and the GaAs surface. In terms of milling depth, the greater the number of loops used, the deeper the milling.

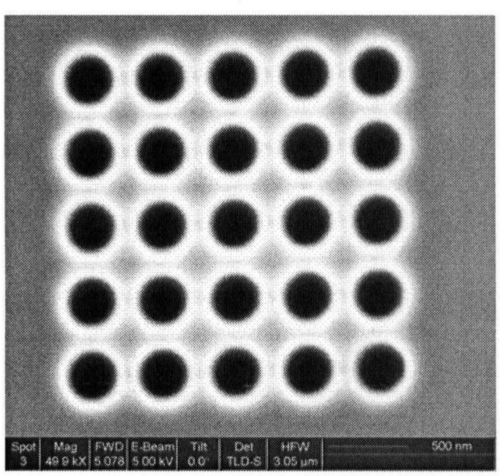
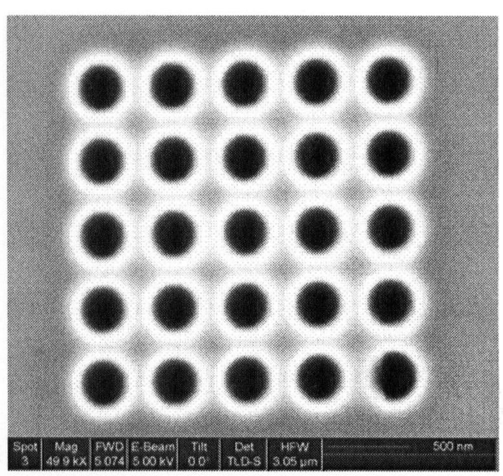

(a) (b)

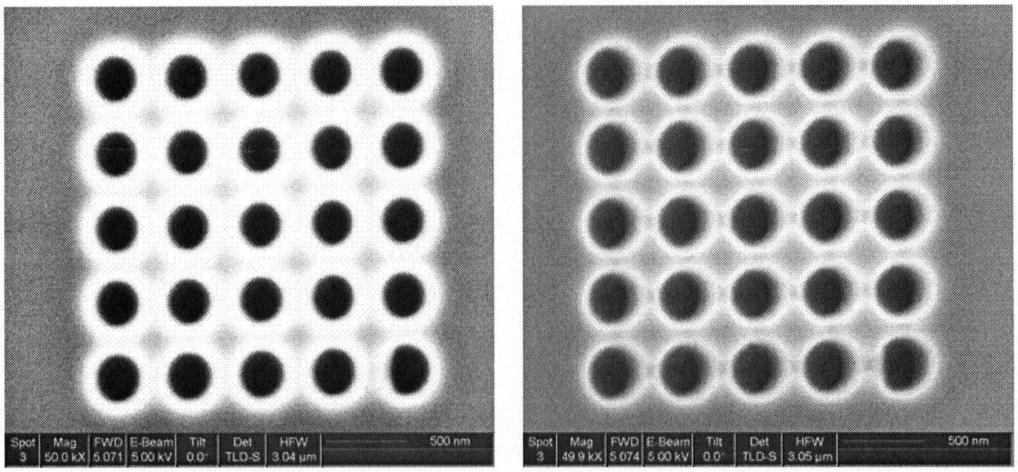

(c) (d)

Fig. 3.6. SEM images of 25 photonic crystal arrays after milling with a dwell time of (a) 0.5 microseconds, (b) 0.7 microseconds, (c) 1 microseconds, and (d) 1.5 microseconds.

To observe the side view of the patterns, we first make a rectangular hole in the wafer and then pattern 100 arrays, in such a way that some patterns could be overlapped with it, as shown in Fig. 3.7 (a) and (c).

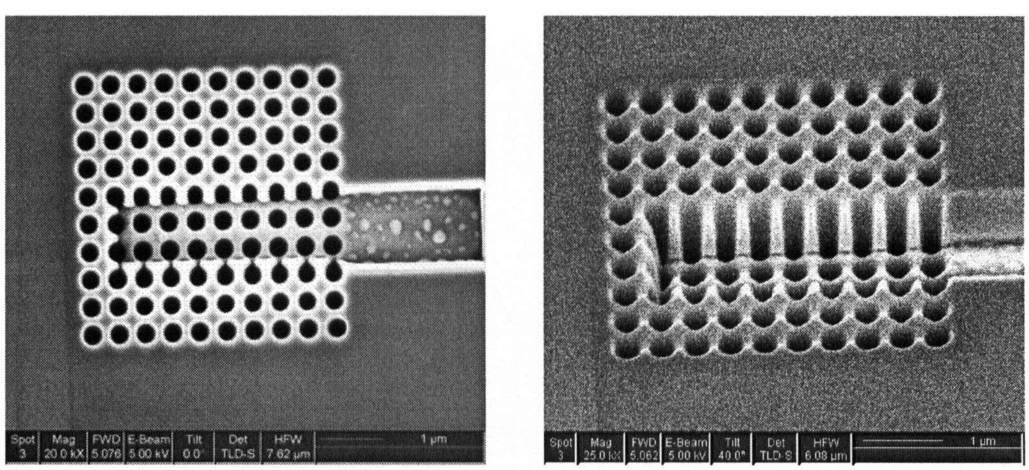

(a) (b)

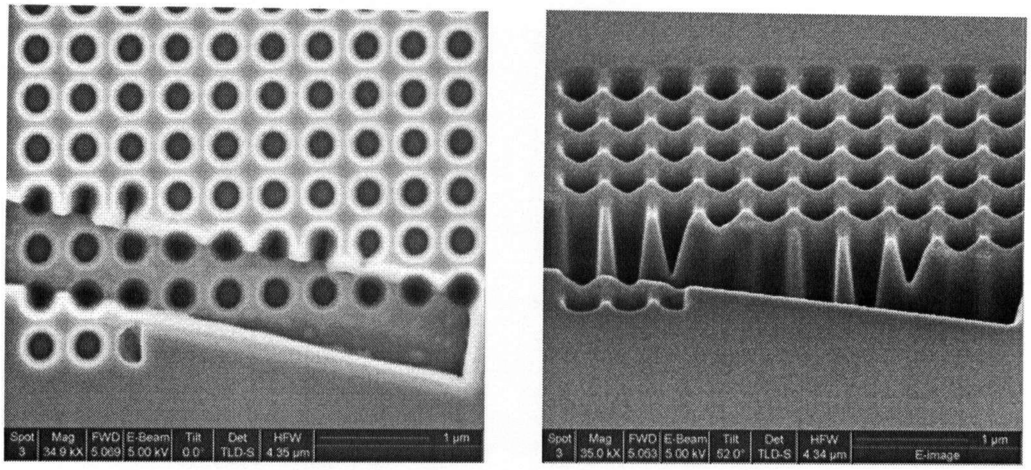

(c) (d)

Fig. 3.7. (a) Top view of overlapping, (b) cross section of holes with 1 microseconds dwell time and 5 loops, (c) Top view of overlapping and (d) cross section of holes with 0.5 microseconds dwell time and 5 loops.

Cross-sections of the patterns with 5 loops after drilling for 1 and 0.5 microseconds dwell time are shown in Fig. 3.7(b) and (d), respectively. Milling is apparently deep enough (>250nm) for the thickness of our photonic crystal slab in both cases. In order to be able to more accurately control the drilling depth, one needs to alter the dwell time and the number of loops.

Despite the benefits of direct milling of FIB, we have found that several points should be taken into consideration for it to be suitable for photonic crystal patterns. First, as a consequence of using gallium ions for drilling, it is difficult to avoid rounded holes (Fig. 3.7 (b) and (d) vividly show uneven surfaces). As well, since ions are hitting the surface everywhere, defects are created, that might absorb light. Second, as shown in Fig. 3.7 (d), the holes are actually cone shaped; if the light is vertically incident to a photonic crystal slab, this cone shape could change the characteristics of guided resonances due to a different size of holes on the top and bottom slab. Third, with the additions of loops and sequences in the stream files, it takes substantial time to make the patterns. For instance, our experiments tell us that it took 6 minutes to write 5um x 5um sized patterns, which means that more than 8 hours are required to make patterns more than 50um x 50um. Milling time could be reduced by decreasing the magnification in addition to the number of loops, but the quality of patterns may have to be compromised. Finally, redeposition of the milling does not make holes uniformly patterned.

3.2.2 E-beam lithography & dry-etching

We use PMMA (Polymethyl Methacrylate) as a photoresist, which is deposited by the spinner at 8000rpm for 40 seconds on the surface of a sample. The thickness of the PMMA after spinning around the center is roughly 500 ~ 550nm. Then we bake the wafer at 180°C for 2 minutes for the PMMA to be solid.

E-beam lithography is done by JEOL SEM. The line dose could vary depending on the probe current (acceleration voltage is fixed to 20KV). Proper line doses and a probe current suitable for photonic crystal patterns of a=446nm and r=180nm (r=0.40a) are tested by varying the parameters and are summarized in Table 3.1.

Table 3.1. Photonic crystal patterns with varying line doses and a probe current of SEM.

Magnification	Line doses (nC/cm)	Probe current (pA)	Patterns after dry-etching
1,000	0.45 ~ 0.60	7	Good
1,000	0.25 ~ 0.40	7.75	Very weakly made
1,000	0.45 ~ 0.60	8	Holes are connected to each other
1,000	0.20 ~ 0.50	10	Holes are connected to each other
1,000	0.20 ~ 0.25	15	Holes are connected to each other

We have found a line dose of between 0.4 and 0.6nC/cm at a 7pA probe current provides very good results. Unless both parameters are appropriately set, after dry-etching, patterns are either very weakly made (either the line dose or probe current is too weak) or collapse (either the line dose or probe current is excessive). Post-patterning, the PMMA is developed under MIBK+IPA (3:1) for 1 minute, followed by IPA for 30 seconds.

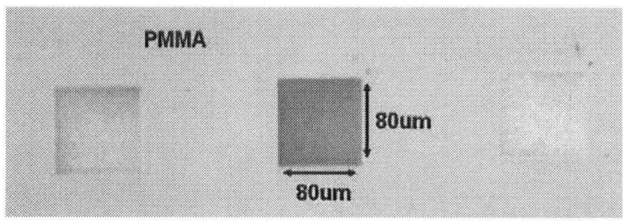

Fig. 3.8. A square lattice of photonic crystal patterns after e-beam lithography. The size of each square is 80um x 80um.

To dry-etch GaAs that lie on a AlGaAs layer, gas mixtures of $SiCl_4$ / SF or BCl_3 / SF_6 are reported to have good selectivity [7-9], but BCl_3 / Ar plasma could be also used to achieve a high etch rate with smooth sidewalls [6]. The etch rate of GaAs under BCl_3 / Ar discharges (1 mTorr, -150 Vdc, 200 W microwave) are proportional to the amount of BCl_3 in the gas mixtures [6].

Etch rates between the PMMA and $Al_{0.12}Ga_{0.88}As$ under various BCl_3 plasma with Ar are tested to find the optimum gas condition and are summarized in Table 3.2. The temperature, pressure, RF power and microwave power of ECR are set to 10°C, 7mTorr, 10W, and 100W, respectively, by referring to our GaAs suspended SWG fabrication [5]. According to our test results, 4 sccm BCl_3 flow rate with 8 sccm Ar works very well for 230nm substrate etching (however, the etch rates could be measured differently in each trial). After dry-etching, the remaining PMMA can be removed by immersion in acetone for 5 minutes.

Table 3.2. Etch rates with varied flow rate of BCl_3.

Ar (sccm)	BCl_3 (sccm)	Etch rate (PMMA : $Al_{0.12}Ga_{0.88}As$)	Comments
8	2	2 : 1	PMMA is completely etched away during the dry-etching
8	4	1 : 2.4	Good
8	8	1 : 1.6	Erosion rate of PMMA is considerable

SEM images of holes after dry-etching are shown in Fig. 3.9. The depth of a single hole is also measured by AFM in Fig. 3.10, which is about 250nm and slightly deeper than our $Al_{0.12}Ga_{0.88}As$ substrate.

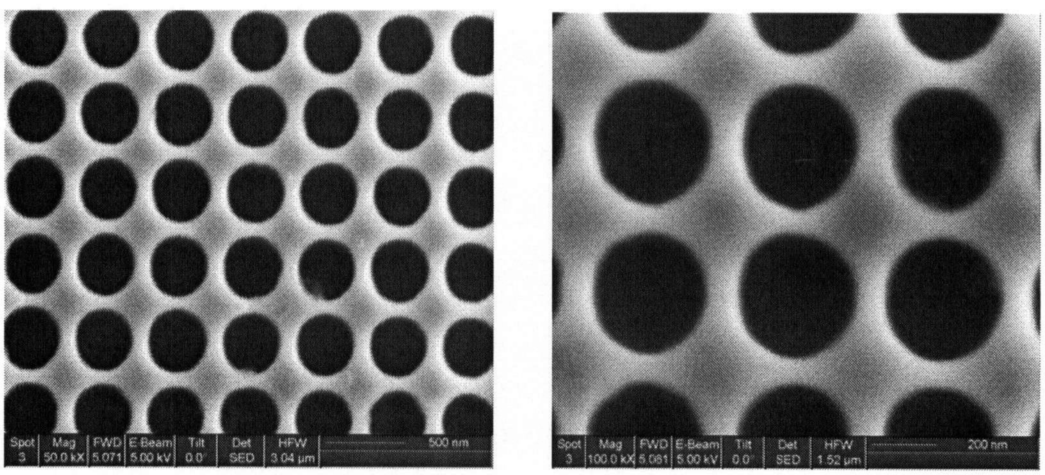

Fig. 3.9. SEM images of holes designed for a=446nm and r=180nm taken after dry-etching.

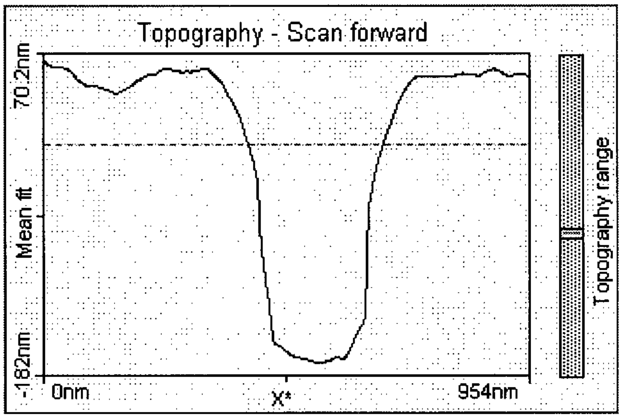

Fig. 3.10. Measurement of the depth of a hole by AFM scanning.

3.3. Removal of sacrificial layer

The sacrificial layer, a 480nm thick $Al_{0.9}Ga_{0.1}As$, could be removed by Buffered Oxide Etch (BOE). Putting the sample in 1:25 BOE: H_2O solution for 2 minutes can etch 480nm $Al_{0.9}Ga_{0.1}As$ sufficiently [10]. After BOE, the sample is thoroughly rinsed with DI water and IPA, then the suspended membrane is relieved by a Tousimis Autosamdri-815 Critical Point Drier (CPD). Critical point drying is to reduce the surface tension to zero so that membranes do not stick to each other and are not deformed in the process of drying. The sample is immersed in a CPD chamber filled with ultra pure alcohol, and LCO_2 gas is then mixed with the alcohol to reach critical point (pressure: 1350psi and temperature: 31 °C). Under the 5 minutes purge time, critical point drying is maintained for 4 minutes, then the alcohol and LCO_2 gas are removed.

In Fig. 3.11, SEM images of the sample after BOE for 2.5 minutes and CPD are shown. The $Al_{0.9}Ga_{0.1}As$ sacrificial layer is completely etched away and the membrane can now be suspended.

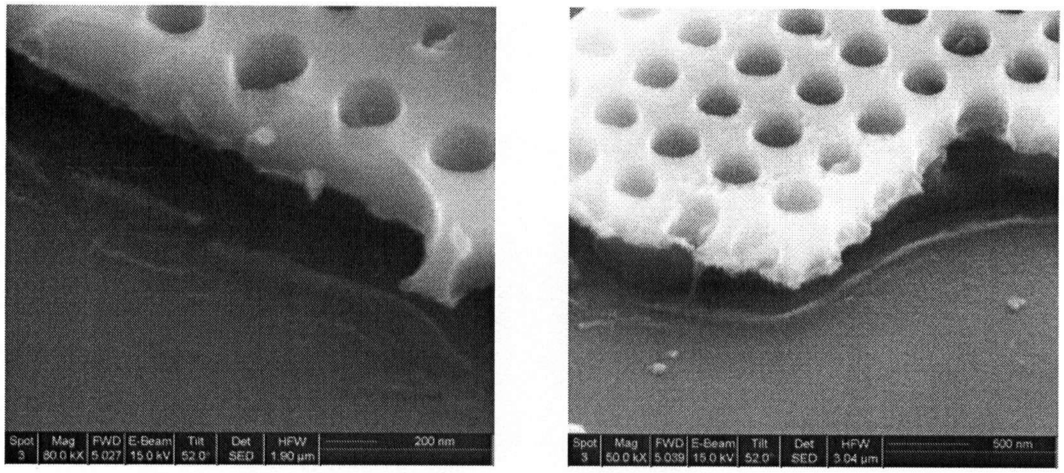

Fig. 3.11. SEM images show a suspended membrane after BOE & CPD.

Although the BOE and CPD work very well to remove the sacrificial layer, Fig. 3.12 and Fig. 3.13 show that membranes eventually collapse after these processes. Alternative methods, therefore, to prevent suspended membranes from being damaged should be discussed.

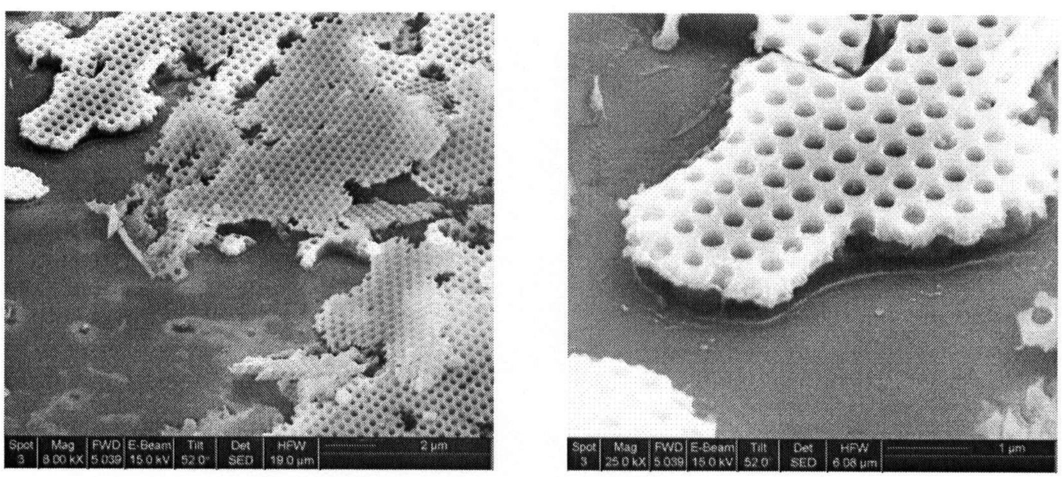

Fig. 3.12. Membranes are broken after BOE & CPD (sample made by e-beam & dry-etching).

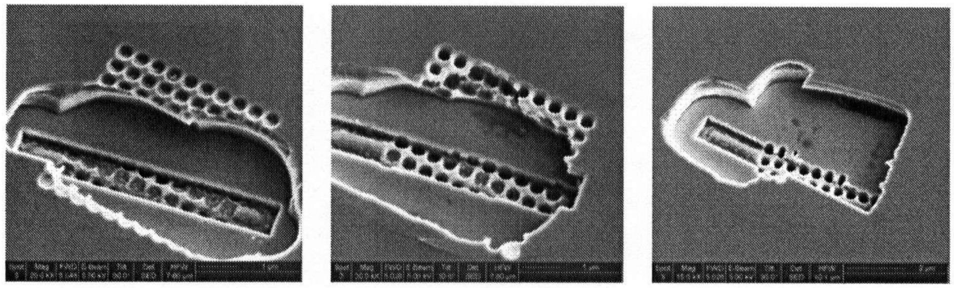

Fig. 3.13. Membranes are broken and lifted off after BOE & CPD (sample made by FIB milling).

3.4. Conclusion

Despite its ease of use, FIB milling is not an appropriate method for writing photonic crystal patterns because re-deposition prevents very sharp features from being made. On the other hand, e-beam writing (line dose between 0.4 to 0.6nC/cm at a 7pA probe current) & dry-etching (4 sccm BCl_3 and 8 sccm Ar) give good results. Since the total size of patterns ($\approx$ 80um x 80um) is very small compared to the size of a sample ($\approx$ 5mm x 5mm), patterns could be uniformly made by e-beam lithography. As well, as a result of using a resist mask, the surface of the sample is not damaged during these steps, as it is in FIB drilling.

The sacrificial layer is removed under 1:25 BOE(1:7): H_2O and the suspended membrane is released by CPD. BOE for 2 ~ 2.5 minutes works well for etching 480nm $Al_{0.9}Ga_{0.1}As$ without substantial undercut. On the other hand, membranes are very fragile and broken into pieces after BOE & CPD, so new techniques should be investigated to complete suspended photonic crystal arrays.

References

[1] T. Stomeo, G. Visimberga, M.T. Todaro, A. Passaseo, R. Cingolani, M. De Vittorio, S. Cabrini, A. Carpentiero, and E. D. Fabrizio, “Rapid prototyping of two-dimensional photonic crystal devices by a dual beam focused ion beam system,” Microelectronic Engineering, pp 417-421, 2005.

[2] C. Bell, G. Burnell, D.-J. Kang, R.H. Hadfield, M.J. Kappers, M.G. Blamire, Nanotechnology 14, 2003.

[3] T. Schenkel, V. Radmilovic, E.A. Stach, S.-J. Park, A. Persaud, Journal of Vacuum Science & Technology B 21 (6), 2003.

[4] S. Noda, A. Chutinan, M. Imada, Nature 407, 2000.

[5] E. Bisaillon, D. Tan, B. Faraji, A. G. Kirk, L. Chrowstowski, and D. V. Plant, “High reflectivity air-bridge subwavelength grating reflector and Fabry-Perot cavity in AlGaAs/GaAs,” Optics Express, vol. 14, pp. 2573-2582, 2006.

[6] S. J. Pearton, W. S. Hobson, C. R. Abernathy, F. Ren, T. R. Fullowan, A. Katz, and A. P. Perley, “Dry Etching Characteristics of III-V Semiconductors in Microwave BCl_3 Discharges,” Plasma Chemistry and Plasma Processing, vol. 13. no. 2, 1991.

[7] S. Salimian and C. B. Cooper II, J. Electrochem. Soc. 136, 2420, 1989.

[8] C. B. Cooper III, S. Salimian, and H. MacMillan, Appl. Phys. Lett. 51, 2225, 1987.

[9] S. Salimian, C. B. Cooper, III, R. Norton, and J. Bacon, Appl. Phys. Lett. 51, 1083, 1987.

[10] J. Kim, D Lim, and G. M. Yanga, “Selective etching of AlGaAs/GaAs structures using the solutions of citric acid/H2O2 and de-ionized H2O/buffered oxide etch,” J. Vac. Sci.

Technol. B: Microelectronics and Nanometer Structures. vol 16. pp. 558-560, 1998.

Chapter 4. Conclusion and Future Work

4.1. Conclusion

A phase methodology to effectively predict resonant wavelengths of FP cavity structures has been demonstrated, and fabrication of a resonant cavity detector with square-lattice photonic crystal arrays has been described.

FDTD phase analysis was found to be very effective for estimating resonance conditions, compared to the FDTD reflectance method, when the total phase response of the FP cavity structure is varied.

Variation of lithographic parameters, (α , Λ, r, a) in the SWG or Phc VCSEL gives rise to resonance tuning, and the tunability could be achieved up to 60nm (SWG VCSEL) and 87nm (Phc VCSEL), while relatively high cavity Qs (>1,000) are maintained. Considering that current MEMS-based VCSELs need the application of a tuning voltage but offer relatively limited tuning ranges, lithographic tuning by arrays of gratings or photonic crystals could be a good approach to enhance the resonance tunability.

Fabrication of photonic crystal arrays (a=446nm and r=180nm) on a 230nm thick $Al_{0.12}Ga_{0.88}As$ suspended membrane has been demonstrated. Photonic crystal patterning performed by e-beam writing & dry-etching shows higher quality patterns than does FIB milling; a 480nm thick $Al_{0.9}Ga_{0.1}As$ layer under the slab is removed by 1:25 BOE: H_2O for 2.5 minutes. Fabrication steps and optimum recipes for JEOL SEM, ECR, BOE, and CPD have also been determined and described in detail. Regarding the membrane collapse, three ways to resolve the issue are described as future work.

In conclusion, this thesis suggests the possibility of tunable structures for selective multi-wavelength emission or detection, ranging from 800nm to 900nm, by lithographically tunable square-lattice photonic crystal arrays that obtains high quality factors.

4.2. Future Work

Four recommendations to continue the work of this project are as follows.

First, as noted in the last section of Chapter 3, membranes made by either e-beam & dry-etching or FIB milling are eventually broken after BOE & CPD. Several ways to improve the results are as below.

1) Write photonic crystal patterns onto a "C" shaped square so that surface tension does not play too much role in the membrane and patterns as shown in Fig. 4.1.

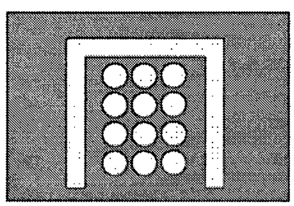

Fig. 4.1. Patterns are written onto the "C" shaped square.

2) Make a smaller number of holes at the edge of the square that helps every corner more robust.

3) Make a small circle by e-beam lithography on a wafer after PMMA and transfer the

hole to be reached until the sacrificial layer. Remove the sacrificial layer by BOE, then write patterns on the surface again by e-beam lithography and dry-etching. By doing so, air membrane can be made prior to patterning.

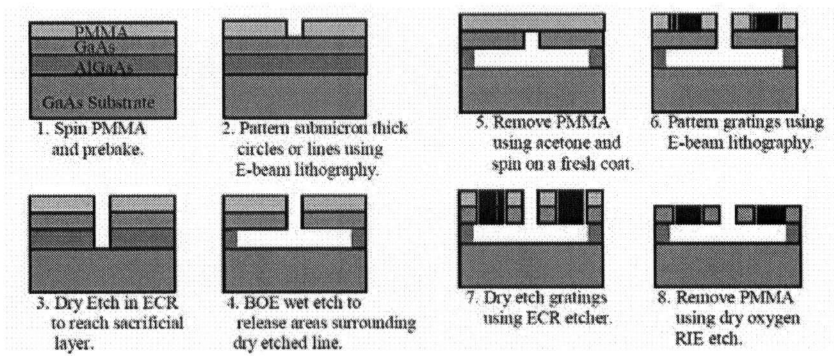

Fig. 4.2. E-beam lithography & dry-etching after removal of the sacrificial layer (From reference [1]).

4) Re-design the lithographic parameters of the photonic crystal slab. In this thesis, the radius of the air hole starts from 0.40a and is increased up to 0.49a, and the size of holes is quite larger than conventional values (typically less than 0.37a). In order to have a more robust membrane, the reduction of the hole size would be necessary.
5) Optimization of CPD settings; i.e., turn the FILL metering valve down to 0.10 rather than the current 0.40 position prior to pushing the FILL button at the onset of the process. As soon as the pressure reaches ~ 700-800psi, slowly open the FILL valve again to the 0.40 setting. This will dampen the effect of the initial incoming LCO2 from atmosphere to operating pressure. As well, we can more slowly decrease the pressure from 1,350psi at critical point, so the membrane damage is minimized.
6) Choose $Al_{0.3}Ga_{0.7}As$ as a Phc slab (or SWG) and GaAs as a sacrificial layer. For this

design, photonic crystal arrays on the $Al_{0.3}Ga_{0.7}As$ slab can be dry etched under BCl_3 / Ar. The GaAs sacrificial layer is then dry etched under BCl_3 / SF_6 while almost no dry-etching of the $Al_{0.3}Ga_{0.7}As$ is expected [4]. A main benefit of this design is to remove the sacrificial layer by dry-etching not by the BOE, so the membrane can be more robust during the fabrication process.

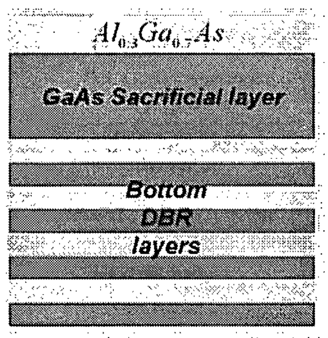

Fig. 4.3. A proposed new wafer design. $Al_{0.3}Ga_{0.7}As$ and GaAs are used for the Phc slab and the sacrificial layer, respectively.

Second, experimental measurements on reflectivities from the resonant structures are the most important task to be performed. On the basis of previous experience with SWG measurements, reflectivities can be measured using either white light or laser as a light source. The resonant wavelengths experimentally observed should be compared with the simulation results, and discrepancies, if present, discussed.

Third, as suggested in Section 3.5, the use of the newly designed wafer, with an increased air gap with 30.5 bottom DBR pairs, would be beneficial to enhance the resonance tunability.

Finally, for the purpose of biosensing applications, Double Band Mirror (DBM) should be taken into consideration. The DBM was proposed by [2,3] where incident optical energy is being reflected, so the 1/3 of the pump power can be recycled. For the wavelength detection from fluorophores, AlN and AlGaN could be used to construct DBRs. However, due to the small difference of the refractive indices between two materials, the DBR stopband is only ~20nm. The DBM is designed by the variation of the thicknesses of DBR pairs that gives rise to splitting of the DBR stopband with two or more at specific wavelengths.

Table 4.1. Emission wavelengths from fluorophores

Fluorophore	Emission (nm)	Fluorophore	Emission (nm)
Alexa 430	545	HEX	556
Alexa 488	516	SYBR Green	520
Alexa 594	612	6- TAMRA	580
Cascade Blue	425	TET	538
Cy3	570	Texas Red	615
Cy5	670	6- ROX	602
Cy5.5	694	Rhodamine	575
JOE	548	Rhodamine Green	527
FAM	518	Rhodamine Red	590

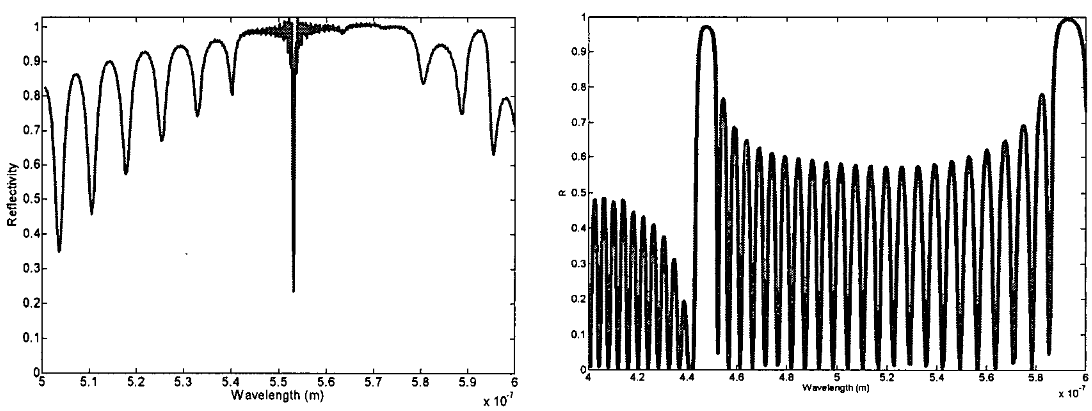

Fig. 4.4. (a) A sharp resonance peak at 553nm is observed over the DBR stopband, 540nm to

560nm. The resonant detector design is based on AlN/AlGaN DBRs with a AlGaN Phc slab and (b) an example of DBM for the emission wavelength at 450nm and 590nm.

In Fig. 4.4(a), a resonant wavelength at 553nm is detected by a FP cavity structure formed by 60 AlN/AlGaN DBR pairs, a 480nm air gap, and a 200nm thick AlGaN Phc slab. Fig. 4.4(b) shows an example of the DBM where the DBR stopbands are located at around 450nm and 590nm, respectively.

References

[1] D. Tan, N. R. Zangenberg, T. Tiedje, L. Chrostowski, E. Bisaillon, D. V. Plant, "A Novel Method for Fabrication of Free Standing Sub-Wavelength Gratings and High Aspect Ratio Cantilevers in GaAs," *Canadian Conference on Electrical and Computer Engineering,* May 2006.

[2] M. Hetterich, M. D. Dawson, A. Y. Egorov, and H. Riechert, "Optically pumped lasing at 1.3um of GaInNaAs-based VCSEL's structures," in *Proc. of 25th International Conf. on Physics and Semiconductors*, vol. 87, Springer Proceedings in Physics, Osaka, 2000, pp. 693-694.

[3] S. Calvez, D. Burns, and M. D. Dawson, "Optimization of an Optically Pumped 1.3-um GaInNAs Vertical-Cavity Surface-Emitting Laser," IEEE Photonics Technology Letters, pp. 1-3, 2002.

[4] S. J. Pearton, W. S. Hobson, C. R. Abernathy, F. Ren, T. R. Fullowan, A. Katz, and A. P. Perley, "Dry Etching Characteristics of III-V Semiconductors in Microwave BCl_3 Discharges," Plasma Chemistry and Plasma Processing, vol. 13. no. 2, 1991.

Appendices

Appendix A. Quantum efficiency of a resonant cavity detector

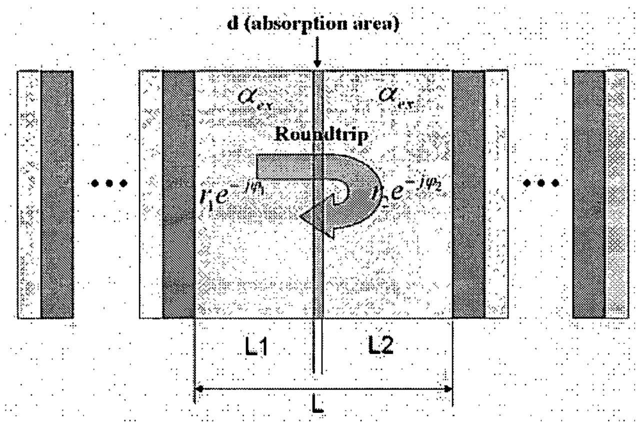

Fig. A.1. The structure of the resonant cavity detector for analysis.

The resonant cavity detector is formed on the basis of a Fabry-Perod (FP) cavity (two mirrors and a cavity in between). Distributed Bragg Reflectors (DBRs) are generally used for the top and bottom mirror to achieve high reflectivities.

In Fig. A.1, an analysis model for the resonant cavity detector is shown. DBRs are used for the top and bottom mirror, and the active layer (thickness = d and absorption coefficient $=\alpha$) is placed in between. Here, r_1, r_2 and φ_1, φ_2 are defined as reflection coefficients and phase shifts imparted by the top and bottom DBR, respectively. L_1 (or L_2) is the distance from the top DBR (or bottom DBR) to the active layer, and α_{ex} is an absorption coefficient in the region of L_1 and L_2.

The quantum efficiency (η) of the structure shown in Fig. A (a) can be written as [5]

$$\eta = \left\{ \frac{(e^{-\alpha_{ex}L_1} + e^{-\alpha_{ex}L_2} R_2 e^{-\alpha_c L})}{1 - 2\sqrt{R_1 R_2} e^{-\alpha_c L} \cos(2\beta L + \varphi_1 + \varphi_2) + R_1 R_2 e^{-2\alpha_c L}} \right\} \times (1 - R_1)(1 - e^{-\alpha d}) \tag{2}$$

where β is a wave number ($\beta = 2n\pi / \lambda$). Since the absorption coefficient α_{ex} ($\approx 5-10cm^{-1}$) in L_1, L_2 is usually far less than the absorption coefficient in the active layer α ($\geq 10^4 cm^{-1}$), Equation (2) can be further simplified by neglecting the α_{ex}, as below [14] :

$$\eta = \underbrace{\left\{ \frac{(1 + R_2 e^{-\alpha L})}{1 - 2\sqrt{R_1 R_2} e^{-\alpha L} \cos(2\beta L + \varphi_1 + \varphi_2) + R_1 R_2 e^{-2\alpha L}} \right\}}_{\textbf{(I)}} \times \underbrace{(1 - R_1)(1 - e^{-\alpha d})}_{\textbf{(II)}} \tag{3}$$

Therefore, if the physical dimensions of the cavity, including the active region and the absoption coefficient in the active layer, are fixed, the quantum efficiency (η) is strongly dependent of the reflectivities of the top and bottom mirror and the wavelengths of the incident wave. In particular, the term $2\beta L + \varphi_1 + \varphi_2$ in equation (3) refers to the wave roundtrip condition in the cavity, so the quantum efficiency η is maximized at resonances periodically (i.e., $2\beta L + \varphi_1 + \varphi_2 = 2\pi m$ ($m = 0, \pm 1, \pm 2 \cdots$)), while being decreased at off resonances (i.e., $2\beta L + \varphi_1 + \varphi_2 \neq 2\pi m$ ($m = 0, \pm 1, \pm 2 \cdots$)). In other words, the constructive (or destructive) interferences at resonances (or at off-resonances) imply the feasibility of the wavelength-selective detection.

When the physical dimensions and the material property are fixed (here αd), the quantum efficiency (η) tends to be higher at resonance, or the reflectivity of the top mirror becomes higher. As well, since the higher mirror reflectance means a higher *Finesse* ($=\frac{\pi\sqrt{R}}{1-R}$), the channel discrimination in Dense Wavelength Division Multiplexing (DWDM) can be improved. In Equation (3), note that the term **(II)** represents the quantum efficiency of the conventional photodetector without the cavity, as shown in Equation (1). Therefore, term **(I)**, added as a result of using the resonant cavity structure enables improvement of the quantum efficiency.

Appendix B. Cavity Q measurement techniques

Here, we introduce three different techniques for measuring quality factors (cavity Qs) in a resonator using FDTD simulations.

First, the FDTD provides a specific method of measuring the Q factor. To do so, the resonator should contain a time monitor inside the cavity and a resonant frequency should be excited by a dipole source. The time monitor records fields as a function of time, displaying the slope of a log-scaled envelop of the field decays as shown in Fig. B.1.

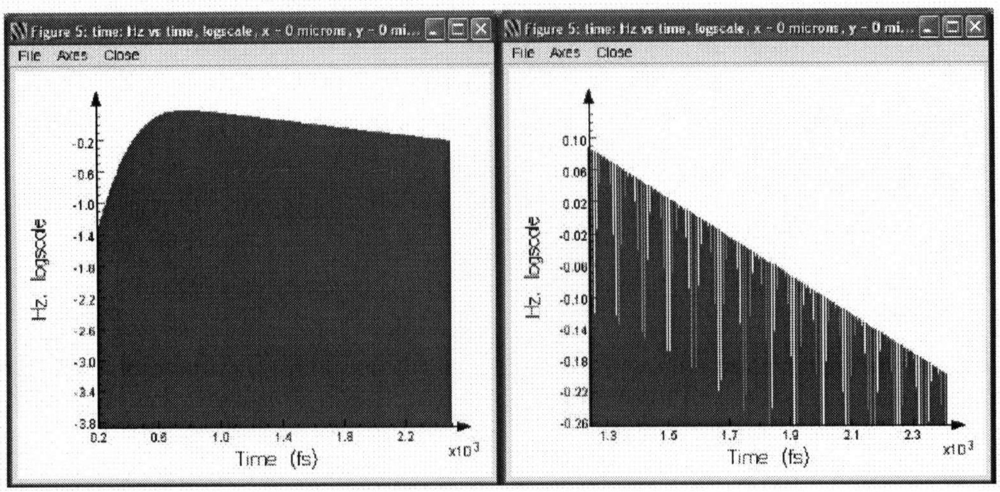

(a) (b)

Fig. B.1. (a) The log-scaled envelop of field decays recorded in a time monitor and (b) zooming in the envelop (From reference [3]).

After measuring the slope of the envelop, we can use the following formula to estimate the cavity Q, as in [3] :

$$Q = \frac{-2\pi \log_{10}(e) f_{resonance}}{2m} \quad \text{(where } m\text{= the slope)} \qquad (5)$$

Second, the cavity Q can be directly measured from a FP peak using the formula $\frac{\Delta\lambda}{\lambda_{resonance}}$ (where, $\Delta\lambda$ is the FWHM of the spectra). For instance, if the resonant wavelength is 850nm and the FWHM of the spectra is measured to 0.5nm, the cavity Q is about 1,700.

Finally, the cavity Q can be calculated by the following formula [2,4] :

$$Q = \frac{v_0}{\Delta v} Finesse \tag{6}$$

where v_0 = resonant frequency, Δv = mode spacing, and *Finesse*= $\frac{\pi\sqrt{R}}{1-R}$.

For the analysis of VCSEL structures, we will use the last method to estimate the cavity Qs. A Problem with the first method is that the resonant frequency can not be correctly excited by a dipole source. As well, if the resonance is excited by the external plane wave, the slope of the envelop of the field decays is not uniform enough to be measured. For the second method, the resolution for the appearance of FP peaks from the FDTD simulations is relatively limited. Particularly, for very high cavity Qs. According to our simulation results, the maximum cavity Q that can be measured by $\frac{\Delta\lambda}{\lambda_{resonance}}$ can not exceed 2,000.

When dealing with the DBR case, since the phase changes versus wavelengths, an effective mirror length l_{eff}, representing field penetration depth of the incident wave into the DBR, should be defined for the sake of an accurate Q calculation. Therefore, the total effective cavity length is defined as $L_{eff} = L + l_{eff,top} + l_{eff,bottom}$.

In Fig. B.2(a), the cavity length is intentionally increased ($20\lambda_{design}$) to measure the effective cavity length of the conventional VCSEL. This structure is composed of 20 $Al_{0.12}Ga_{0.88}As$ and $Al_{0.9}Ga_{0.1}As$ DBR pairs for the top and bottom mirror, respectively, and a $Al_{0.12}Ga_{0.88}As$ cavity. In Fig. B.2(b), several FP peaks are shown in the DBR stopband.

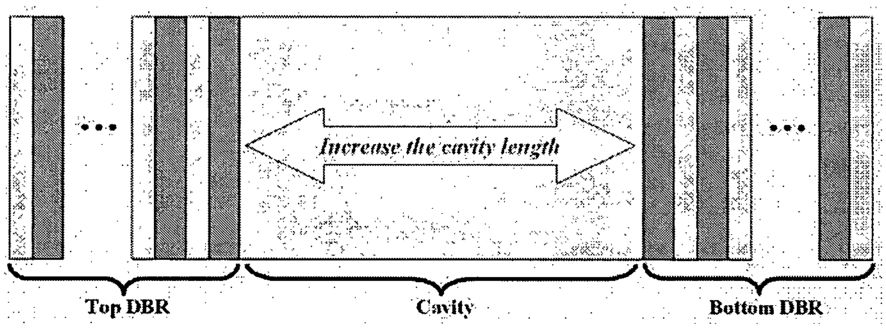

(a)

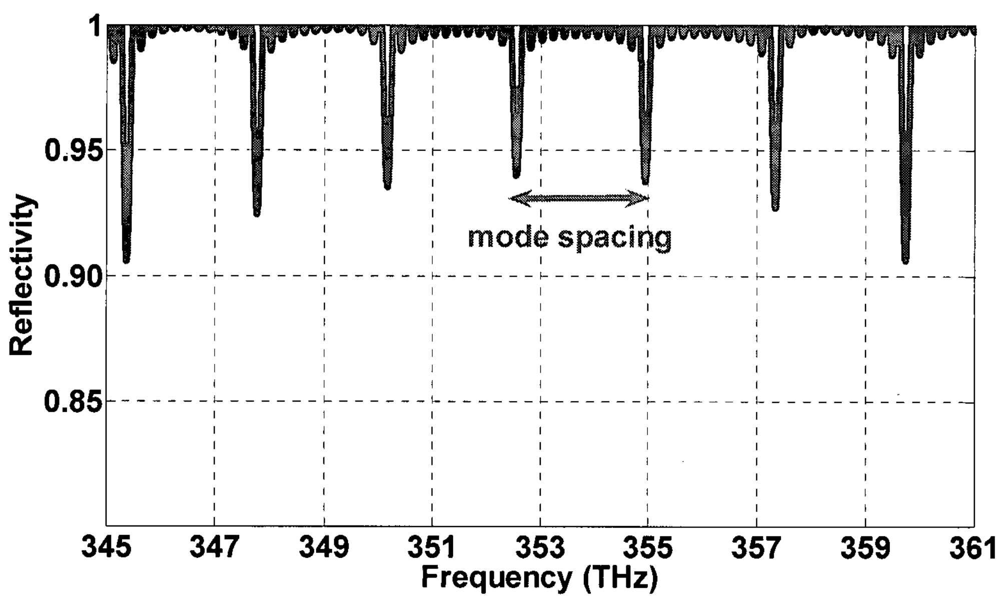

(b)

Fig. B.2. (a) A schematic of the VCSEL structure with increasing cavity length to $20\lambda_{design}$

and (b) resonant frequencies shown in the stopband.

Since we consider the penetration depth of the DBR pairs, L_{eff} can be calculated by $L_{eff} = \frac{c}{2n\Delta v}$. Then, the penetration depths of the two DBRs are $l_{eff,top} + l_{eff,bottom} = \frac{c}{2n\Delta v} - L$. If the two DBRs are identical, l_{eff} can be written as $l_{eff} = \frac{1}{2}(\frac{c}{2n\Delta v} - L)$. According to our simulation result in Fig. B.2(b), the mode spacing between FP peaks is measured at about 2.39THz. Therefore, the l_{eff} (either for the top or bottom DBR) is $l_{eff} = \frac{1}{2}(\frac{c}{2n\Delta v} - L) \cong 400nm$ (where n= refractive index of $Al_{0.12}Ga_{0.88}As$ and c= speed of light).

Therefore, for the conventional VCSEL structure, we can modify the equation (6) as

$$Q = v_0 \left[\frac{2\left\{nL + n_{eff,DBR}(l_{eff,top} + l_{eff,bottom})\right\}}{c} \right] Finesse \qquad (7)$$

where $n_{eff,DBR}$ is the weighted average of DBR materials and $l_{eff,top} = l_{eff,bottom}$.

Similarly, the effective cavity length for the SWG or Phc VCSEL can be calculated for cavity Q calculations. Using Equation (7), cavity Qs for different VCSEL structures are estimated in Chapter 2.

References

[1] K. Kishino, M. S. Unlu, J.-I. Chyi, J . Reed, L. Arsenault, and H. Morkoq, "Resonant Cavity -Enhanced (RCE) Photodetectors," IEEE Journal of Quantum Electronics. vol. 27. no. 8. pp. 2025-2034, 1991.

[2] H. A. Haus, "Waves and Fields in Optoelectronics," Presentice-Hall, Englewood Cliffs, N.J., 1984.

[3] FDTD Solutions user's manual (www.lumerical.com), Lumerical Solutions, Inc., 2006.

[4] A. Yariv, "Optical Electronics in Modern Communications," Oxford University Press, 1997.